1
2
Title: Cryo-EM structure of an elusive pre-transport intermediate of the multidrug transporter BmrCD reveals modes of asymmetric drug binding

3

4
5
Authors: Tarjani M. Thaker[1*], Smriti Mishra[2*], Wenchang Zhou[3], Jose D. Faraldo-Gomez[3], Hassane Mchaourab[2,#], Thomas M. Tomasiak[1,#]

6
Affiliations:

7
[1]Department of Chemistry and Biochemistry, University of Arizona, Tucson, AZ, USA

8
9
[2]Department of Molecular Physiology and Biophysics, Vanderbilt University, Nashville, TN, USA

10
11
[3]Theoretical Molecular Biophysics Laboratory, National Heart, Lung, and Blood Institute, National Institutes of Health, 50 South Drive, Bethesda, MD 20892, USA

12
*These authors contributed equally to this work

13
#Correspondence to: tomasiak@arizona.edu; hassane.mchaourab@vanderbilt.edu

14

15
16
17
18
19
20
21
22
23
24
25
26
27
28
29
30
31
32
33
34
Abstract: Vectorial substrate efflux by ATP binding cassette (ABC) transporters, which play a major role in multidrug resistance, entails the ATP-powered interconversion of the transporter between stable intermediates. Despite recent progress in structure elucidation of ABC transporters, a number of such intermediates have yet to be visualized and mechanistically interpreted. Here, we combine single particle cryo-EM, Double Electron Electron Resonance (DEER) spectroscopy with Molecular Dynamics simulations to profile and mechanistically frame the conformation of a hitherto unobserved intermediate in the context of BmrCD, a heterodimeric multidrug ABC exporter from *Bacillus subtilis.* In our cryo-EM structure, BmrCD adopts an inward facing architecture bound to both ATP and the substrate Hoechst-33342 and is capped by an extracellular domain which undergoes ATP-dependent conformational changes. A striking feature of the structure is a symmetric arrangement of the nucleotide-binding domain (NBD) in the presence of ATP whereas binding of Hoechst at two distinct sites in an acidic pocket stabilizes an asymmetric arrangement of the transmembrane domain architecture (TMD). Mutation of residues coordinating Hoechst in the structure abrogates the cooperative stimulation of ATP hydrolysis. In conjunction with previous studies, our findings suggest a mechanistic role for symmetry mismatch between NBDs and TMDs in the conformational cycle of ABC transporters. Moreover, the resolved structures of bimodally-bound drugs are of notable importance for future rational design and optimization of molecules for targeted transport inhibition of ABC transporters.

35
36
One Sentence Summary: Cryo-EM and EPR analysis reveal cooperative substrate binding in BrmCD in an architecture primed for transport.

ATP binding cassette (ABC) transporters harness the energy of ATP hydrolysis to traffic molecules across lipid membranes. Ubiquitous in all kingdoms of life, ABC exporters efflux a spectrum of substrates, most notably cytotoxic drugs[1]. Although the molecular architecture of ABC transporters invariably has two nucleotide binding domains (NBD) with two ATP binding sites (also referred to as the nucleotide binding site (NBS)) and two transmembrane domains (TMDs), a subfamily has evolved a catalytically-impaired NBD. Typically assembled as heterodimers, ABC exporters of this subfamily are distinguished by an asymmetric duty cycle of the motor domain where ATP hydrolysis is primarily carried out by the active ATP binding site[1], also known as the consensus NBS. The mechanistic implications of the asymmetric ATP turnover continue to be an active area of investigation.

Owing to the widespread application of single particle cryo-EM, the structural biology of ABC exporters has witnessed rapid advances in the last few years yielding snapshots of transporters in distinct conformational states. Most notably, a complement of such states was resolved for a bacterial ABC heterodimer, TmrAB[2]. These included inward-facing (IF), occluded and outward-facing (OF) conformations, and for the first time a post-hydrolysis low energy state where asymmetric binding of ATP and ADP was resolved. Current models of ATP-driven transport posit that ABC transporters rest in an inward-facing open conformation with NBDs slightly separated for high affinity substrate and nucleotide binding, though recent studies report nucleotide binding in this architecture is constitutive at least in exporters[1]. The ATP-substrate-transporter complex is then in a state favorable for transport once both NBDs are aligned to form an intact ATP hydrolysis pocket. Conserved loops (Walker A, Walker B, P-loop), present in most ATPases, and motifs (Q-loop) that are specific only to ABC transporters coordinate the positioning of a catalytic water by a highly conserved glutamate residue in the Walker B motif resulting in ATP hydrolysis and the subsequent reset of the transport cycle.

Despite the success of the TmrAB investigation in linking intermediates of ATP hydrolysis to distinct conformations, significant mechanistic gaps remain. One critical gap pertains to the sequence of events that occur prior to transition to OF conformations after substrate and ATP binding. Except ABC homodimers, structures of ATP-bound ABC exporters almost invariably have been obtained in a catalytically-impaired background where both NBD catalytic glutamates were replaced with glutamines[2–4]. Moreover, these structures as well as those of ATP-bound TmrAB, capture outward facing or occluded conformations[3–8]. This has led to a generalized conclusion that ATP binding stabilizes the OF conformation despite evidence that the stability of such a conformation may be transporter dependent[9]. Furthermore, prior to this transition, a loaded IF intermediate bound to substrate and ATP must be postulated. Such an intermediate could be transient for TmrAB, explaining its absence in the cryo-EM maps.

A second, heterodimer-specific mechanistic gap, pertains to the nature of drug binding. Efforts to sensitize drug-resistant cells to various small molecules and chemotherapeutics by inhibiting efflux pumps such as heterodimeric ABC transporters has not yet proven successful[10,11]. In the absence of a detailed understanding of determinants of transporter/drug interactions, progress on this front remains stalled. Some insights have emerged from recent structures of P-glycoprotein (Pgp) visualizing substrates[12] and inhibitors[13] cradled in the vestibule between the TMDs with

stoichiometries of one and two per transporter, respectively. In contrast, the peptide substrate was poorly resolved in TmrAB structures precluding an analysis of the role of asymmetry in heterodimer substrate recognition, although substrate binding shifted the equilibrium towards a more open IF conformation[2].

To address these two central mechanistic gaps, we integrated cryo-EM with Double Electron Electron Resonance (DEER) spectroscopy, Molecular Dynamics (MD) simulations and biochemical analysis to determine, validate and mechanistically contextualize a pre-transport, ATP-bound, Hoechst-loaded intermediate of the ABC heterodimer BmrCD from *Bacillus subtilis*. BmrCD was selected on the basis of previous DEER analyses demonstrating that the ATP-bound IF intermediate is relatively stable[14,15]. We further stabilized this intermediate in a catalytically-impaired mutant background where putative catalytic residues in both NBDs have been replaced with glutamine. Hoechst is transported by BmrCD in inside-out-vesicles and stimulates ATP turnover of the purified transporter in detergent micelles and nanodiscs[16]. The transporter structure adopts an inward-facing conformation characterized by symmetric, yet disengaged NBDs, but structurally asymmetric transmembrane domains. DEER distributions in the mutant background reveal that the cryo-EM conformation is a minor population in the ensemble. Notably, the cryo-EM maps reveal two antiparallel Hoechst molecules bound in the IF cavity, making contacts primarily with BmrC protomer seemingly reflecting the internal symmetry of the protein structure. Micro-second MD trajectories are consistent with this interpretation, and reveal the network of polar and aromatic interactions that stabilizes both substrate molecules concurrently. The predicted binding mode and stoichiometry of Hoechst is further interrogated by functional analysis and determination of Hill coefficients in wild-type (WT) BmrCD. We found that Hoechst-mediated stimulation of ATP hydrolysis is cooperative, and mutation of residues in contact with the Hoechst molecules blunts stimulation of ATP hydrolysis. In conjunction with DEER analysis, our structure integrates a number of recent results and fills in a key gap in the mechanistic understanding of ATP-coupled conformational dynamics of ABC exporters.

RESULTS
The structure of BmrCD in the substrate and ATP-bound state adopts an inward-open architecture

The structure of BmrCD was determined using single particle cryo-electron microscopy (**Fig. 1A-C; Table 1; Supp. Fig. 1**) of a Cysteine-less (C-less) BmrCD bearing glutamine substitution of D500 in BmrC and E592 in BmrD (referred to hereafter as BmrCD-QQ). The transporter was purified into LMNG micelles which were subsequently exchanged for digitonin micelles to facilitate orientation distribution on cryo-EM grids (see methods). BmrCD-QQ for cryo-EM structure determination was pre-saturated with excess ATP and Hoecsht-33342 in order to stabilize the ligand-bound intermediate (see methods). From a final dataset consisting of nearly 4.3 million, we determined a structure to 3.5Å resolution from a final subset of 157,021 particles in an inward-facing conformation where the extracellular side is closed. The topology of the entire architecture is revealed in sufficient detail to identify the presence of two molecules of the model substrate Hoechst in a central vestibule of the TMD and a single molecule of ATP in each NBD (**Fig. 1B, Supp. Fig. 2**). Notably, we resolve the architecture of a TMD insertion in

127 BmrD, between TM2 and TM3, forming an extracellular cap over the extracellular gate of
128 BmrCD which we define as the BmrCD extracellular domain (ECD) (**Fig. 1D**). Comparison
129 of the observed geometry to the series of inward-facing structures of the closely related
130 exporter TmrAB highlights a wider IF architecture in BmrCD with NBDs slightly separated
131 (**Fig. 2A**) relative to the narrow inward-facing open (IFnarrow; PDB ID 6raf[17]) (RMSD
132 5.424 Å) or the inward-facing wide conformation of TmrAB (IFwide; PDB ID 6rag[17]; RMSD
133 3.624 Å), both of which are stabilized by nucleotide binding in the NBS (**Supp. Fig. 3**,
134 **Supp. Table 2**). In comparison to other prokaryotic exporters of known structure[2,6,18–24]
135 and related members of the ABCB[3,13,25] and ABCC[4,5] families, BmrCD geometry is most
136 similar in architecture to the heterodimeric exporter TM287/288 asymmetrically bound to
137 AMP-PNP in one NBS (PDB ID: 4q4a[22]; RMSD 3.135 Å) (**Supp. Fig. 4, 5**). However, the
138 conformation of BmrCD is unique in that it is both substrate and ATP-bound yet is inward-
139 facing.

140 **The ATP and Hoechst-bound IF conformation has symmetric but disengaged NBDs**
141 Because previous structures of catalytically impaired ABC transporters have
142 captured occluded or OF conformations[3,4,6], we characterized the ensemble of
143 conformations using DEER distance measurements between pairs of spin labels in the
144 impaired BmrCD-QQ background for protein solubilized in digitonin and ß-DDM micelles.
145 Consistent with these previous studies, distance distributions in the TMD (spin label pairs
146 96/188 and 55/146) report a predominantly OF conformation in the presence of Hoechst
147 and ATP although a minor IF population, which we presume is captured in the cryo-EM
148 structure, is evident in the distance distributions (**Fig. 1D**). Corresponding DEER
149 distributions in the WT BmrCD background previously published are shown for
150 reference[14].
151 The structure presented here features symmetric NBDs, and NBSs (**Fig. 2A-C**),
152 consistent with DEER data (**Fig. 2D**). Distance distributions between spin labels
153 introduced in proximity to the degenerate (348/532) and consensus (440/441) ATP
154 binding sites for the QQ background are similar to those obtained in the Vanadate-trapped
155 intermediate of WT BmrCD (**Fig. 2D**). As previously observed for the EQ double mutants
156 in P-glycoprotein (Pgp)[3], the D500Q and E592Q mutations present in BmrCD-QQ
157 abrogate the asymmetry of the NBS observed under turnover conditions (solid green
158 traces in Figure 2D) in the C-less background. The distance distributions at the NBS pairs
159 predicted from the structure overlap with those experimentally observed in C-less BmrCD
160 in the presence of AMP-PNP (dashed green traces in **Figure 2D**). In the structure, the
161 geometry of ATP binding is also symmetric and adopts nearly identical conformations
162 (**Fig. 2B,C**). The unambiguous density into which ATP was modeled appears in a
163 canonical site for nucleotide binding that overlaps with ATP in TmrAB[2] and AMP-PNP in
164 TM288/287[26]. In this orientation, the Walker A motif stabilizes the β−phosphate of ATP,
165 whereas the Glutamine residue in place of the catalytic base is oriented towards the γ-
166 phosphate in both protomers (**Fig. 2C**). Unexpectedly, the NBDs of BmrC of BmrD do not
167 contact each other, and nucleotide binding is supported entirely by intra-domain
168 interactions that stabilize ATP within a well-defined cleft. These results support the
169 following two conclusions: 1) The NBD architecture of our structure is more consistent
170 with inward-facing open populations of BmrCD that are stabilized by non-hydrolyzable

171 AMP-PNP and 2) this state is more symmetric in the NBDs than in WT BmrCD in the
172 presence of Hoechst and ATP.

Architecture and ATP-dependent dynamics of the ECD domain

174 A unique feature that distinguishes BmrCD from other biochemically-characterized
175 ABC exporters, is the presence of an insertion between transmembrane helix 1 (TM1)
176 and transmembrane helix 2 (TM2), which we define as the extracellular domain (ECD).
177 Electron Potenial Density corresponding to the ECD reveals a primarily β-stranded
178 domain consisting of two approximate subdomains (**Fig. 1D; 3A**). The ECD is positioned
179 in an orientation that results in extensive interactions with the TMD thereby occluding the
180 extracellular TMD bundle of both BmrC and BmrD. Analysis of the electrostatic
181 distribution over the surface of the ECD and at ECD/TMD interface further reveal both
182 acidic and basic patches that extend into the TMD (**Fig. 3B,C**). Notably, an acidic stretch
183 of residues extends from the ECD to the BmrC TMD; whereas, the ECD/TMD interface in
184 BmrD is marked by a basic stretch. Somewhat surprising is the formation of a solvent
185 accessible, acidic cavity in the ECD. Binding of both Hoechst molecules in the BmrCD
186 TMD is observed in a similarly acidic vestibule (see below), suggesting translocation of
187 substrate through the TMD may proceeds via interaction with and rearrangement of the
188 ECD.
189 We tested the notion of a functional role for the ECD by measuring distances
190 between a spin label on this domain (BmrD 126) relative to the two spin labels monitoring
191 the extracellular packing of BmrC (55) and BmrD (146) (**Fig. 3D**). The ECD/BmrC
192 interface site (46/126) undergoes a large amplitude distance opening in the high-energy
193 post hydrolysis state (red traces in **Figure 3**). Similarly, the 55/126 pair report a large
194 distance change as would be expected if the ECD moved in concert with BmrD. On the
195 other hand, we observed a small distance change between the BmrD TMD (146) and the
196 ECD (126) suggesting ATP-coupled rearrangement of this domain within the BmrD
197 protomer.

The ATP and Hoechst-bound IF conformation features asymmetry of the transmembrane domain

200 Similar to TmrAB and TM287/288, BmrC and BmrD come together to form a
201 vestibule presumably to enable substrate binding. However, this assembly is asymmetric
202 in the TMD of BmrCD (**Supp. Table 1**). Superposition of the BmrD TMD onto the BmrC
203 TMD by rotation around the pseudosymmetric axis of the TMD dimer highlights an
204 outward shift of nearly every TM in BmrC relative to BmrD on the extracellular side (**Fig.
205 4A**). The arrangement of the intracellular side of the TMD bundle is similarly marked by
206 a concerted outward movement of all BmrC TM helices relative to BmrD. The intracellular
207 side also exhibits the most substantial reorientations, specifically of TM3, 4, and 6 in BmrC
208 which shift away from the substrate binding cavity by ~4Å relative to BmrD. The presence
209 of several π-helices along the TMD bundle likely accommodates the independent
210 movement of the TMD helices on the two sides of the membrane leaflet.
211 Comparison of the pseudosymmetric arrangement of the TMD in BmrCD to TmrAB
212 TMD highlights similarities to wild-type TmrAB in the nucleotide-bound wide state (PDB
213 ID: 6rag[2]) and the EQ variant in the apo state (PDB ID: 6ran[2]) (**Supp. Table 2**). Even in
214 these related architectures, substantial differences are observed in nearly every TM of

215   BmrD compared to TmrA, the equivalent canonical chain in TmrAB. Comparison of the
216   TMD geometry to inward-open architectures observed in related ABC exporters further
217   highlights the asymmetry of the BmrCD TMD halves (**Supp. Fig. 5**). The structures of
218   both apo and AMP-PNP-bound TM287/288 bear the strongest resemblance to the
219   BmrCD TMD geometery[22,27]. Superposition of each half independently reveals nearly
220   identical bundles in BmrC and TM287, both of which contain the non-canonical NBS and
221   is the site of bound nucleotide in both structures (AMP-PNP in TM287). However, a
222   comparison between the homologous BmrD and TM288 chains reveals a smaller
223   interhelical angle between TM4/TM6 in BmrD (~50º) than in BmrC or TM287/TM288
224   (~60º). These differences could be due to interactions between the BmrD ECD and TMD
225   bundle, or to the unique features of substrate binding in the BmrCD TMD.

226   **Asymmetric binding sites of two Hoechst molecules in the TMD**
227   Remarkably, density was observed in the TMD vestibule that is able to
228   accommodate the assignment of not just one but two molecules of Hoechst. Calculation
229   of a cross-correlation score was used to rationalize a parallel or antiparallel arrangement
230   of the two molecules, with the latter scoring higher (0.65 (antiparallel) versus 0.60
231   (parallel)) and thus supporting an antiparallel assignment. Notably, the TMD substrate
232   densities exhibit an asymmetric positioning relative to the pseudosymmetric axis of the
233   TMD (**Fig. 4B**), matching the asymmetry of the TMDs. The Hoechst molecules bind in an
234   opposite orientation to each other, an arrangement similar to the Pgp inhibitors
235   zosuquidar and tariquidar in Pgp[28,29]. The Hoechst binding pockets are on each side of a
236   secondary pseudosymmetric two-fold axis relating the NBDs and are lined with residues
237   primarily along the BmrC half of the TM bundle. These pocket-lining residues differ
238   between the two halves, ie they are in non-equivalent from BmrC to BmrD (**Fig. 4H-I**),
239   likely because the TMD segment lining the substrate vestibule itself is asymmetric (**Fig
240   4A**; **Supp. Fig. 5**). Nonetheless, BmrC residues L130, F134, and W290 line both pockets.
241   Also, both pockets form a chemically similar environment, lined by aromatic residues
242   (pocket 1 – Phe293; pocket 2 – Phe83 and Phe134) and capped by an acidic residue
243   (pocket 1 Glu297; pocket 2 – Asp141).

244   **Antiparallel Hoechst molecules are stabilized by analogous interaction patterns**
245   To evaluate the interpretation of the distinct densities observed within the BmrCD
246   transmembrane domain as two antiparallel Hoechst molecules, and to identify the specific
247   interactions that underpin their stabilization, we turned to all-atom molecular dynamics
248   (MD) simulations (**Fig. 4E**). Specifically, we calculated two independent 1-µs trajectories
249   in which the transporter and the two Hoechst molecules are free to diffuse, or reconfigure,
250   and evaluated the resulting structure in each case. For computational efficiency, we
251   considered a protein construct that lacks the nucleotide-binding domains and the ECD
252   inserted between TM1 and TM2 of BmrD was also truncated (**Fig. 4E**). In the cryo-EM
253   structure, these domains contribute minimally to the BmrC-BmrD interface, which
254   primarily involves contacts in the transmembrane domains. The simulated construct
255   showed a high degree of similarity to the starting structure throughout the calculated
256   trajectories, with average backbone RMSD values of 1.6 ± 0.2 Å over the last 0.5 µs (**Fig.
257   5F**). The two Hoechst molecules initially modeled also remained stably bound, each
258   forming multiple contacts with BmrC, but barely any with BmrD (**Figs. 4G,4H,4I Supp.**

259   **Fig. 6**). For both molecules, the two simulations resulted in similar poses and interaction
260   patterns; this convergence is reassuring as it indicates both MD trajectories sample the
261   same energetically favorable states. The information from the MD trajectories was used
262   to fit the Hoechst molecules in cryo-EM density for an optimal placement.
263   Unlike the two molecules of ATP in the BmrCD NBSs, the two molecules of
264   Hoechst are marked by different geometries (**Fig. 4C**). Hoecsht-1 (silver) is largely
265   coordinated by residues from BmrC TM3, TM5 and TM6 and one residue from BmrD TM1
266   and 2 residues from BmrD TM6 (**Fig. 4H**) whereas Hoecsht-2 (green) forms extensive
267   contacts with residues primarily from BmrC TM1, TM2, and TM3 (**Fig. 4I**). The binding
268   pose for Hoechst-1 appears to be defined by the interaction between the piperazine group
269   (carrying a charge of +1) and Glu297 (**Fig. 4G**). The two benzimidalole rings (which
270   together also carry a charge of +1) form additional π-π and cation-π interactions with the
271   rings of Phe293 and Trp290, whereas the etoxy-benzene is engaged by a T-shaped
272   aromatic interaction with Tyr257. Hoechst-2, while oriented inversely relative to the
273   membrane plane, is similarly anchored by ion-pairing and cation-π interactions formed by
274   the piperazine group, namely with Asp141, Phe145 and Trp290, which is the only residue
275   that contacts both ligand molecules in our trajectories. The benzimidalole rings in
276   molecule '2' form additional π-π and cation-π interactions with the rings of Phe83 and
277   Phe134, whereas the etoxy-benzene tail appears to be largely disengaged, in contrast to
278   Hoechst-1 (**Fig. 4G**). These interactions, π-π and cation-π interactions, are reinforced by
279   their observation in the cryo-EM structure. Interestingly, therefore, the pattern of
280   interactions formed by the two molecules in this antiparallel arrangement also appears to
281   reflect the internal structural symmetry of the TMDs.
282   Lastly, it is worth noting that these interaction patterns recapitulate what is
283   observed in high-resolution crystal structures of other biomolecules in complex with
284   Hoechst. In the In the outward-open structure of the MFS-family multi-drug transporter
285   LmrP[30], a Hoechst molecule is stabilized through ion-pairs between two acidic side chains
286   and the piperazine and benzimidalole groups, albeit in a different orientation nearly
287   perpendicular to the plane of the transmembrane. The ligand is however only in contact
288   with one of the transmembrane domains, like in our structure of inward-open BmrCD.
289   Binding of Hoechst to LmrR, a transcriptional repressor of the LmrCD drug transporter,
290   involves aromatic stacking of tryptophan sidechains and the benzimidalole rings[31], while
291   dipole-π and water-mediated polar interactions explain the mode of binding to DNA[32]. Our
292   cryo-EM and MD simulation data shows that it is this interaction versatility that may enable
293   BmrCD to recognize two Hoechst molecules simultaneously.
294   Moreover, the arrangement and asymmetry in geometry of the two Hoechst
295   molecules in the cryo-EM structure and MD analysis are not without precedent and are
296   reminiscent of the two molecules of the inhibitor zosuquidar bound to human Pgp[13]
297   (ABCB1) where one zosuquidar molecule is extended while the other molecule is in a
298   slightly bent conformation (**Supp. Fig. 5**). Notably, binding of these inhibitors occurs at a
299   site closer to the extracellular gate, which potentially supports the occluded architecture
300   observed in Pgp. The positioning of Hoechst in BmrCD-QQ is most similar to LPS bound
301   to MsbA and overlaps with the inner core of the polysaccharide portion of the molecule
302   (**Supp. Fig. 5**)[20], parallel with the presumed inner leaflet of the transmembrane region.

303

Cooperative Hoechst stimulation of ATP turnover is blunted by mutation of coordination residues

Because our structure reveals the presence of two bound Hoechst molecules, we reasoned that mutual stabilization would result in cooperative binding of the drug. To test this notion, we determined the k_{cat} of BmrCD ATP hydrolysis as a function of increasing Hoechst concentrations (**Fig. 5A**). We observed a sigmoidal dependence of k_{cat} with a Hill coefficient of approximately 1.8 (**Fig. 5B**). Not only does this data confirm cooperativity, but it also mechanistically validates the binding of two Hoecsht molecules by demonstrating direct coupling to ATP hydrolysis to the NBDs.

Conversely, mutations of residues that coordinate the substrate molecules in the structure reduce stimulation of ATP turnover (**Fig. 5C**). We targeted both acidic and hydrophobic residues in the cavity. Alanine substitution effects were variable but overall consistent with the residues implicated in the structure. Notably, W290A which coordinates both Hoechst molecules has a substantial effect on ATP stimulation. Similarly, D141 in proximity to Hoechst-2 abrogates the Hoechst dependence, although its basal rate is higher than for WT BmrCD. This presumably reflects a rearrangement of the BmrC molecules that disrupt coupling of the TMD to the NBD.

DISCUSSION

The accelerated pace of structure determination of ABC exporters set the stage for an almost unprecedented structure-mechanism understanding. Yet intermediates predicted to be populated in the transport cycle continue to be conspicuously absent from the structural record. In addition, except for TmrAB and bacterial homodimers, the structure space has been dominated by transporters with impaired ATP-hydrolysis. In the presence of ATP, these structures are outward-facing with no evidence of bound substrates. Based on spectroscopic[14,33] and biochemical data[34], the underlying mutations conspire to reshape the energy landscape further confounding the mechanistic interpretation of the structural record.

The collection of TmrAB cryo-EM structures is thus far the most complete record of stable intermediates on the energy landscape of an ABC exporter. However, under turnover conditions of excess ATP, two predicted intermediates were missing. One is the OF conformation which purportedly release the substrate, the absence of which was attributed to its presumed transient nature. The structure of the OF conformation was visualized in the catalytically-impaired mutant bound to ATP as well as in the vanadate-trapped WT. The second, is a loaded pre-transport intermediate poised for transition to the high energy OF conformation. Because previous structures of catalytically-impaired ABC exporters such as Pgp[3] and Mrp1[4] were in the OF conformations, a substrate- and ATP-loaded IF intermediate was not accounted for.

Here, we report the structure of this elusive substrate- and ATP-bound, intermediate. Cryo-EM reveals an IF architecture bound with to molecules of the substrate Hoecst-33342 in the TMD, and two molecules of ATP in the NBDs of a catalytically impaired variant of BmrCD. Each molecule of Hoechst binds in a similarly located but nonequivalent pocket on the C or D chain and our ATPase data support their role in cooperative allosteric modulation of ATP turnover. Validated by DEER measurements in

the WT and the mutant, we assign this conformation to the substrate- and ATP-loaded intermediate poised for transition to a high energy post hydrolysis intermediate. In the case presented here, previous DEER data highlighted the stability of the ATP-bound IF intermediate in BmrCD which was one of two fortuitous factors that allowed it to be represented in our cryo-EM reconstruction, although outward facing states may also be present. The second factor is the structural order of this intermediate which was conducive to it cryo-EM reconstruction.

Our BmrCD structure unlocks details of the nature of pseudosymmetry breaking in ABC transporters and stimulates hypotheses on the mechanistic roles of symmetry mismatch between the NBDs and TMDs. Alignment with the recently determined cryo-EM structures of TmrAB confirms that BmrCD is in a previously unobserved intermediate. Distances between NBDs are most consistent with the inward-facing wide state, albeit BmrCD is wider than TmrAB. Approximately 75% of BmrCD aligns with this TmrAB conformation, including all of BmrC and most of the transmembrane portion of BmrD. The NBD of the canonical BmrD protomer does not align, instead showing a ~40° rotation around the symmetry axis of the NBD dimer.

The symmetry of the NBDs holds for most of the transmembrane region but is broken in several locations including TM3 and TM6, especially TM6 in BmrD. TM6 is noteworthy because this helix has been identified as important for substrate gatekeeping in TmrAB[35] and in *C. elegans* Pgp[36]. In our structure, TM6 in BmrC and BmrD each directly binds one of the two Hoechst molecules which are located in similar pockets in BmrC and BmrD, showing a pseudo-symmetric arrangement. However, TM6 from BmrC breaks that symmetry and is closer to TM6 of BmrC. MD simulations confirm this arrangement and the stabilizing interactions that overlap with the binding mode observed in the structure. We propose a direct relationship between the asymmetry of substrate binding in the cavity and the overall asymmetry of the TMDs of BmrCD.

An emerging theme from structural and spectroscopic investigations of ABC exporters posits a role for substrates and inhibitors in stabilizing symmetric or asymmetric conformations. Cryo-EM structures of Pgp have highlighted different modes of inhibitors and substrates binding with the former filling more of the substrate cavity and inducing a more symmetric arrangement of the NBDs[12]. However, substrate binding induces asymmetric states both in IF conformations and post-hydrolysis conformations, as deduced from DEER analysis of Pgp[37]. Building on this theme, we propose that our symmetry-mismatched BmrCD structure is arrested in an "inhibited-like conformation" by the substitution of the catalytic glutamate in the consensus NBS. In a WT background, we propose that the asymmetry would propagate from the TMD to the NBD resulting in the asymmetric hydrolysis of ATP during transport. Indeed, extensive DEER investigations of BmrCD under turnover conditions concluded that ATP hydrolysis in the consensus NBS is coupled to asymmetric structure of the NBDs[14]. We predict that subsequent or concurrent transition to an OF conformation accompanied by the dissociation of the substrates resolves the asymmetry in the TMD.

393   In addition to outlining the structural features and the mechanistic context of an
394 intermediate presumed to be poised for transport and revealing modes of substrate
395 interactions with a multidrug transporter, our results have general implications for the field.
396 Our structure resembles a necessary intermediate on the path from structures that have
397 been observed with cryo-EM – a symmetric resting state without substrate loaded to
398 asymmetric post-hydrolysis states that have released substrate. In between these states,
399 a transition must occur that "breaks" this symmetry and bring NBDs into alignment for
400 proper catalysis to take place in one of the two NBDs. This transition may reflect
401 asymmetric loading of substrate and asymmetric movements in the TMDs that
402 allosterically facilitate NBD alignment. BmrCD only has one such functional site, but a
403 similar mechanism may be relevant for most ABC exporters, which have two such sites
404 but which nevertheless might have a preferred order[38]. Nevertheless, the absence of
405 intermediates in the structural record of a particular transporter may reflect the energetic
406 idiosyncrasies of the transporter being investigated and should not be extrapolated in the
407 context of a general mechanism. Thus, a consensus mechanism for ABC heterodimers
408 will require the convergence of structural, spectroscopic and functional investigations of
409 multiple transporters.
410

411 **MATERIALS AND METHODS**

412 **Cloning**

413   Cysteine-less (C-less) BmrCD in pET21b(+) was created as described
414 previously[14]. Briefly, native Cysteines in BmrCD-WT were substituted with alanines using
415 QuikChange site directed mutagenesis. The C-less BmrCD template was then used to
416 generate BmrCD-QQ where the conserved Glutamate of the walker B motif in the
417 consensus site in BmrD (E592) and aspartate of the degenerate site in BmrC (D500) were
418 substituted with Glutamine (Q). Site-directed mutagenesis was also used to generate
419 double-Cysteine mutants and substrate binding mutants. All substitutions were confirmed
420 by DNA sequencing.

421

422 **Expression and purification**

423   Wild-type C-less BmrCD and all mutant plasmids were transformed into
424 *Escherichia coli* BL21(DE3) cells. A single colony was inoculated into 20 mL Luria Broth
425 (LB) for the primary culture which subsequently was used to start the main culture
426 consisting of 1L of minimal media supplemented with glycerol (0.5% v/v), thiamin (2.5
427 µg/mL), ampicillin (100 µg/mL), MgSO$_4$ (1 mM), and 50X MEM amino acids (1 mL).
428 Cultures were grown at 37°C with shaking to an OD$_{600}$ of 1.2, and the expression of
429 BmrCD induced by the addition of 0.7 mM isopropyl β-D-1-thiogalactopyranoside. BmrCD
430 cultures were incubated at 25°C with shaking for another 5.5 h. The cells were harvested
431 by centrifugation and stored at −80°C. The cell pellets were resuspended in 20 mL of lysis
432 buffer (50 mM Tris-HCl, 5 mM MgCl$_2$, 1mM EDTA, pH 7.5), including 10 mM DTT, 10
433 µg/mL DNase, 0.1 mM PMSF, 1/3 of a Complete EDTA-free protease inhibitor cocktail
434 tablet (Roche) and were lysed by five passes through an Avestin C3 homogenizer at 15-
435 20,000 PSI. The lysate was centrifuged at 9,000g for 10 min to remove cell debris and
436 the membranes isolated by ultracentrifugation at ~200,000g for 1 h.

Membranes of C-less BmrCD and mutants assayed in 0.05% n-dodecyl-β-D-maltopyranoside (β-DDM) were solubilized in resuspension buffer (50 mM Tris-HCl, 100 mM NaCl, 15% (v/v) glycerol, pH 8.0) including 1 mM DTT, 1.25 % w/v β-DDM with constant stirring on ice for 1 h. The membranes of double mutants studied in 0.25% digitonin were solubilized in resuspension buffer (50 mM Tris-HCl, 100 mM NaCl, 15% (v/v) glycerol, pH 8.0) including 1 mM DTT and 1% w/v Lauryl Maltose Neopentyl Glycol (LMNG). Solubilized membranes were then centrifuged at 200,000g for 1 h to remove insoluble particulates. The solubilized fraction was then incubated for 2 h with 300 µL of pre-equilibrated Ni-NTA resin (QIAGEN) in Ni-NTA buffer (50 mM Tris-HCl, 100 mM NaCl, 15% (v/v) glycerol, 0.05% β-DDM, pH 8.0) for ß-DDM samples or Ni-NTA buffer 2 (50 mM Tris-HCl, 100 mM NaCl, 15% (v/v) glycerol, 0.005% LMNG, pH 8.0) for digitonin samples. BmrCD-bound Ni-NTA resin was loaded into a gravity column, washed with five column volumes of Ni-NTA buffer containing 20 mM imidazole and eluted with buffer containing 250 mM imidazole.

Cryo-EM sample preparation

C-less BmrCD harboring the D500Q (BmrC) and D592Q (BmrD) mutations (BmrCD-QQ) was prepared cryo-EM by first exchanging sample purified by size exclusion chromatography in SEC Buffer 1 (50 mM Tris-HCl, 150 mM NaCl, 0.01% LMNG, 20% glycerol, pH 7.4) into SEC Buffer 2 (50 mM Tris-HCl, 200 mM NaCl, 0.06% digitonin, pH 7.4). Briefly, approximately 2.5 mg of SEC-purified BmrCD-QQ was buffer exchanged by two rounds of 10-fold dilution with SEC Buffer 2 and concentration in an Amicon Ultra-100 kDa centrifugal filters (Millipore) prior to SEC purification over a Superose 6 Increase column (Cytiva) equilibrated in SEC Buffer 2 (**Supp. Fig. 1**). Fractions were pooled and concentrated to a final concentration of 3.1 mg/mL measured by BCA Assay (Pierce). For substrate trapping, protein was diluted to 22 µM (~2.5 mg/mL) in 50 mM Tris-HCl, 200 mM NaCl, 0.2% digitonin, pH 7.4 and incubated with 75 µM Hoecsht-33342 (Thermo Fisher) on ice for 30 min prior to the addition of 8 mM ATP/MgCl$_2$. To initiate substrate trapping, the sample was then heated for 1 min at 37°C and immediately applied to freshly glow-discharged grids placed inside of a Leica GP2 plunge freezer equilibrated to 10ºC and 85% humidity.

Cryo-EM data acquisition and processing

Cryo-EM data were collected on a Quantifoil 1.2/1.3 200-mesh spacing copper grid (Electron Microscopy Sciences) loaded with 5 µL of BmrCD-QQ saturated with Hoecsht-33342/ATP/MgCl$_2$ (BmrCD-QQ$^{H/ATP}$) and incubated for 10 s prior to blotting on Whatman 1 paper for 4 s and plunge-frozen in liquid ethane. In total, 6,919 were recorded by beam-image shift on a 300 kV Titan Krios microscope (Thermo Fisher) equipped with a K3 Summit detector (Gatan) operated in super-resolution mode (Pacific Northwest Center for Cryo-EM) at a nominal magnification of 81,000X, corresponding to a pixel size of 0.54 Å. Dose-fractionated movies were acquired at an electron flux of 0.82 e^{-1}/Å^2 per frame (45 frames total) corresponding to a total dose of 37.2 e^{-1}/Å^2. Images were recorded with a target defocus range of -0.8 to 2.1 µm.

480   Data were processed in RELION 3.0[39] and 3.1[40]. Frame-based motion correction,
481   2X binning, and dose weighting were performed using MotionCor2 to generate an image
482   stack with pixel size of 1.059 Å. Defocus values were estimated from motion corrected,
483   dose weighted images using CTFFIND4.1[41]. Approximately 1,500 particles were
484   manually picked from an initial subset of micrographs and subject to likelihood-based 2D
485   classification to generate templates for automated particle picking. In total, 4,970,928
486   particles were picked, extracted at a box size of 288 pixels with 4.0 Å/pixel, split into 4
487   subsets of 1,242,732 particles, and subject to four rounds of 2D classification and particle
488   selection to eliminate bad particles resulting in a final particle set containing 632,978
489   particles extracted to the full pixel size (1.059 Å/pix) for 3D classification. The best class
490   selected on the basis of highest resolution and visible transmembrane density yielded
491   157,021 particles, which were then subject to iterative rounds of 3D refinement, CTF
492   refinement, Bayesian polishing, and postprocessing in RELION to yield a final map at 3.5
493   Å resolution as defined by local resolution calculation in RELION 3.1. Masks were
494   generated manually in Chimera[42] from RELION and CisTEM[43] maps. The use of
495   SIDESPLITTER[44] extensions in RELION 3.1 were used in the reconstruction step in later
496   rounds of refinement with a large mask to counter the effects of observed over-fitting to
497   the detergent micelle and to ensure that all map density was included. Data processing
498   details are shown in **Supplemental Figure 1**.
499   Model building was performed was performed in Coot[46] using RELION
500   postprocessed maps with blurring and sharpening as needed performed in CCPEM[45]. A
501   starting structure was generated from TmrAB (PDBID: 6rag[35]) truncated to poly-alanine.
502   Real space refinement was performed using Phenix[47] against RELION postprocessed
503   maps. Secondary structure and reference model restraints were used, as was a high
504   nonbonded energy term to ensure proper geometry. The ISOLDE[48] plug-in to ChimeraX[49]
505   was used for difficult regions and to ensure correct orientation of H-bonds. Placement of
506   the Hoechst molecules was performed manually in Coot and then further refined with MD
507   simulations (see below) and in Phenix. All structure figures were made using ChimeraX
508   and PyMol[50].

509

510   **MD simulations**

511   All simulations were carried out with NAMD 2.12[51] using the CHARMM36 force
512   field[52,53] periodic boundary conditions, constant temperature (298 K) and semi-isotropic
513   pressure (1 atm), and an integration time step of 2 fs. Force-field parameters for Hoechst-
514   33342 were those developed in a previous study[30]. Long-range electrostatic interactions
515   were calculated using PME, with a real-space cut-off of 12 Å; van der Waals interactions
516   were computed with a Lennard-Jones potential cut-off at 12 Å with a smooth switching
517   function taking effect at 10 Å. For computational efficiency, the considered in the
518   simulations comprises only the transmembrane domain, i.e. extracellular (BmrD, residue
519   50-114) and intracellular domains (BmrC, residue 317-574; BmrD, residue 411-665) were
520   truncated. Two molecules of the ligand Hoechst-33342 were included; the initial binding
521   pose was produced by manual-fitting into the cryo-EM density map. The protein-ligand
522   complex was embedded in a pre-equilibrated palmitoyl-oleoyl-phosphatidyl-choline
523   bilayer, in a 100 mM NaCl buffer, using GRIFFIN[51]. Counterions were added to neutralize
524   the net charge of the protein-ligand complex. The resulting system contain 206 POPC

525   lipids and are ~90 x 90 x 126 Å in size, totaling ~106,000 atoms. The molecular system
526   was equilibrated following a staged protocol comprising a series of restrained simulations.
527   The protocol consists of both positional and conformational restraints, gradually
528   weakened over 100 ns, and individually applied to protein sidechains and backbone as
529   well as the Hoechst molecules. Subsequently, two trajectories of 1 μs each were
530   calculated, with no restraints.

531
532   **Spin-labeling of BmrCD**

533   For EPR spectroscopy, double-Cysteine mutants generated on the C-less
534   background of BmrCD were eluted following Ni-NTA purification and labeled with 20-fold
535   molar excess of 1-oxyl-2,2,5,5-tetramethylpyrroline-3-methyl methanethiosulfonate
536   (Enzo Life Sciences) at room temperature in the dark over a 4 h period, after which protein
537   samples were placed at 4 °C overnight (~15 h). The labeled protein samples in ß-DDM
538   and LMNG were then separated from free label by size-exclusion chromatography on a
539   Superdex 200 Increase column (Cytiva) in buffer containing 50 mM Tris-HCl, 150 mM
540   NaCl, 10% (v/v) glycerol, pH 7.4 containing 0.05% β-DDM (ß-DDM samples) or 0.01%
541   LMNG (digitonin samples). The samples in 0.01% LMNG containing buffer were then
542   exchanged into digitonin buffer (50 mM Tris-HCl, 200 mM NaCl, 0.06% w/v digitonin, pH
543   7.4). The collected fractions of spin-labeled BmrCD mutants were concentrated using an
544   Amicon Ultra-100 kDa centrifugal filters (Millipore), and the final concentration determined
545   by absorbance at 280 nm (Mean extinction coefficient = 68077.5 M^{-1} cm^{-1}).

546
547   **DEER sample preparation and DEER spectroscopy**

548   Spin-labeled BmrCD mutants were concentrated to 70-100 μM using Amicon Ultra-
549   100 kDa centrifugal filters (Millipore) and incubated with nucleotides or Hoechst-33342.
550   The final concentrations of ATP, AMP-PNP, vanadate, $MgCl^{2+}$, and digitonin were 10 mM,
551   10 mM, 5 mM, 10 mM, and 0.25% respectively. Samples for DEER analysis were
552   cryoprotected with 24% (v/v) glycerol. Post-hydrolysis (ADP-Vi) and turnover (H-ATP-
553    $MgCl^2$) samples prepared in digitonin buffer were incubated at 37°C for 15 min and 1 min,
554   respectively. β-DDM-solubilized protein samples were trapped in the post-hydrolysis state
555   and with AMP-PNP by incubating at 30°C for 30 min. Turnover samples in β-DDM buffer
556   conditions were incubated at 30 °C for 5min. Post-hydrolysis (ADP-Vi), turnover (H-ATP-
557    $MgCl^{2+}$) and AMP-PNP reactions were stopped by flash freezing in a liquid nitrogen bath.
558   DEER spectroscopy was performed on an Elexsys E580 EPR spectrometer
559   operating at Q-band frequency (33.9 GHz) equipped with a 40W Amp-Q amplifier (Bruker)
560   with the dead-time free four-pulse sequence at 83 K[54,55]. The pulse lengths were 10 ns
561   (p/2) and 20 ns (p) for the probe pulses and 40 ns for the pump pulse. The frequency
562   separation was 73 MHz. Raw DEER decays were analyzed as described previously[14].
563   Briefly, primary DEER decays were analyzed using home-written software operating in
564   the Matlab environment. The software carries out global analysis of the DEER decays
565   obtained under different conditions for the same spin-labeled position. The distance
566   distribution is assumed to consist of a sum of Gaussians, the number and population of
567   which are determined based on a statistical criterion. Distance distributions on the
568   BmrCD-QQ cryo-EM structure were predicted *in silico* using 1 ns molecular-dynamics
569   simulations with dummy spin labels with default parameters using the DEER Spin-Pair

13

570 Distributor at the CHARMM-GUI website[56,57]. Experimental Data related to **Figures 1E**,
571 **2D**, and **3D** are reported in **Supplemental Figure 7**.

572

ATPase assays

574 The specific ATPase activities for wild-type (WT) and mutants of C-less BmrCD
575 were determined by an inorganic phosphate assay as previously described[14] with slight
576 modification. Briefly, BmrCD (20 µg) samples were incubated with increasing
577 concentrations of ATP at 30°C for 30 min under basal conditions (no Hoechst) or
578 presence of different concentrations of Hoechst. The reaction was stopped by adding 1%
579 SDS and the color was developed using a 1:1 solution of ammonium molybdate (2% in
580 1M HCl) and ascorbic acid (12% in 1M HCl). The absorbance of samples was measured
581 at a wavelength of 850 nm on a BioTek Synergy H4 microplate reader. The amount of
582 phosphate released was determined by comparison to a standard curve generated from
583 inorganic phosphate. The Vmax of WT and mutant C-less BmrCD was derived using the
584 Levenberg-Marquart nonlinear least squares fitting approach in Origin (OriginLab, Inc).

585

REFERENCES AND NOTES

1. Holland, I. B. Rise and rise of the ABC transporter families. *Res. Microbiol.* **170**, 304–320 (2019).

2. Hofmann, S. *et al.* Conformation space of a heterodimeric ABC exporter under turnover conditions. *Nature* **571**, 580–583 (2019).

3. Kim, Y. & Chen, J. Molecular structure of human P-glycoprotein in the ATP-bound, outward-facing conformation. *Science (80-.).* **359**, 915–919 (2018).

4. Johnson, Z. L. & Chen, J. ATP Binding Enables Substrate Release from Multidrug Resistance Protein 1. *Cell* **172**, 81-89.e10 (2018).

5. Johnson, Z. L. & Chen, J. Structural Basis of Substrate Recognition by the Multidrug Resistance Protein MRP1. *Cell* **168**, 1075-1085.e9 (2017).

6. Choudhury, H. G. *et al.* Structure of an antibacterial peptide ATP-binding cassette transporter in a novel outward occluded state. *Proc. Natl. Acad. Sci. U. S. A.* **111**, 9145–9150 (2014).

7. Ward, A., Reyes, C. L., Yu, J., Roth, C. B. & Chang, G. Flexibility in the ABC transporter MsbA: Alternating access with a twist. *Proc. Natl. Acad. Sci. U. S. A.* **104**, 19005–19010 (2007).

8. Dawson, R. J. P. & Locher, K. P. Structure of a bacterial multidrug ABC transporter. *Nature* **443**, 180–185 (2006).

9. Mishra, S. *et al.* Conformational dynamics of the nucleotide binding domains and the power stroke of a heterodimeric ABC transporter. *Elife* **3**, e02740 (2014).

10. Tamaki, A., Ierano, C., Szakacs, G., Robey, R. W. & Bates, S. E. The controversial role of ABC transporters in clinical oncology. *Essays Biochem.* **50**, 209–232 (2011).

11. Seelig, A. P-Glycoprotein: One Mechanism, Many Tasks and the Consequences for Pharmacotherapy of Cancers. *Frontiers in Oncology* **10**, (2020).

12. Alam, A., Kowal, J., Broude, E., Roninson, I. & Locher, K. P. Structural insight into substrate and inhibitor discrimination by human P-glycoprotein. *Science (80-.).* **363**, 753–756 (2019).

13. Nosol, K. *et al.* Cryo-EM structures reveal distinct mechanisms of inhibition of the human multidrug transporter ABCB1. *Proc. Natl. Acad. Sci. U. S. A.* **117**, 26245–26253 (2020).

14. Mishra, S. *et al.* Conformational dynamics of the nucleotide binding domains and the power stroke of a heterodimeric ABC transporter. *Elife* **2014**, (2014).

15. Collauto, A., Mishra, S., Litvinov, A., Mchaourab, H. S. & Goldfarb, D. Direct Spectroscopic Detection of ATP Turnover Reveals Mechanistic Divergence of ABC Exporters Article Direct Spectroscopic Detection of ATP Turnover Reveals Mechanistic Divergence of ABC Exporters. *Structure* **25**, (2017).

16. Torres, C., Galián, C., Freiberg, C., Fantino, J.-R. & Jault, J.-M. The YheI/YheH heterodimer from Bacillus subtilis is a multidrug ABC transporter. *Biochim. Biophys. Acta - Biomembr.* **1788**, 615–622 (2009).

17. Zutz, A. *et al.* Asymmetric ATP Hydrolysis Cycle of the Heterodimeric Multidrug ABC Transport Complex TmrAB from *Thermus thermophilus*. *J. Biol. Chem.* **286**, 7104–7115 (2011).

18. Nöll, A. *et al.* Crystal structure and mechanistic basis of a functional homolog of the antigen transporter TAP. *Proc. Natl. Acad. Sci. U. S. A.* **114**, E438–E447

15

641   (2017).
642   19.   Mi, W. *et al.* Structural basis of MsbA-mediated lipopolysaccharide transport.
643   *Nature* **549**, 233–237 (2017).
644   20.   Ho, H. *et al.* Structural basis for dual-mode inhibition of the ABC transporter
645   MsbA. *Nature* **557**, 196–201 (2018).
646   21.   Angiulli, G. *et al.* New approach for membrane protein reconstitution into
647   peptidiscs and basis for their adaptability to different proteins. *Elife* **9**, (2020).
648   22.   Hohl, M. *et al.* Structural basis for allosteric cross-talk between the asymmetric
649   nucleotide binding sites of a heterodimeric ABC exporter. *Proc. Natl. Acad. Sci. U.
650   S. A.* **111**, 11025–11030 (2014).
651   23.   Ward, A., Reyes, C. L., Yu, J., Roth, C. B. & Chang, G. Flexibility in the ABC
652   transporter MsbA: Alternating access with a twist. *Proc. Natl. Acad. Sci. U. S. A.*
653   **104**, 19005–19010 (2007).
654   24.   Dawson, R. J. P. & Locher, K. P. Structure of a bacterial multidrug ABC
655   transporter. *Nature* **443**, 180–185 (2006).
656   25.   Esser, L. *et al.* Structures of the Multidrug Transporter P-glycoprotein Reveal
657   Asymmetric ATP Binding and the Mechanism of Polyspecificity. *J. Biol. Chem.*
658   **292**, 446–461 (2017).
659   26.   Hohl, M. *et al.* Structural basis for allosteric cross-talk between the asymmetric
660   nucleotide binding sites of a heterodimeric ABC exporter. *Proc. Natl. Acad. Sci. U.
661   S. A.* **111**, 11025–11030 (2014).
662   27.   Timachi, M. H. *et al.* Exploring conformational equilibria of a heterodimeric ABC
663   transporter. *Elife* **6**, (2017).
664   28.   Nosol, K. *et al.* Cryo-EM structures reveal distinct mechanisms of inhibition of the
665   human multidrug transporter ABCB1. *Proc. Natl. Acad. Sci. U. S. A.* **117**, 26245–
666   26253 (2020).
667   29.   Alam, A., Kowal, J., Broude, E., Roninson, I. & Locher, K. P. Structural insight into
668   substrate and inhibitor discrimination by human P-glycoprotein. *Science (80-.).*
669   **363**, 753–756 (2019).
670   30.   Debruycker, V. *et al.* An embedded lipid in the multidrug transporter LmrP
671   suggests a mechanism for polyspecificity. *Nat. Struct. Mol. Biol.* (2020).
672   doi:10.1038/s41594-020-0464-y
673   31.   Madoori, P. K., Agustiandari, H., Driessen, A. J. M. & Thunnissen, A. M. W. H.
674   Structure of the transcriptional regulator LmrR and its mechanism of multidrug
675   recognition. *EMBO J.* **28**, 156–166 (2009).
676   32.   Robinson, H. *et al.* 2'-Deoxyisoguanosine adopts more than one tautomer to form
677   base pairs with thymidine observed by high-resolution crystal structure analysis.
678   *Biochemistry* **37**, 10897–10905 (1998).
679   33.   Verhalen, B. *et al.* Energy transduction and alternating access of the mammalian
680   ABC transporter P-glycoprotein. *Nature* **543**, 738–741 (2017).
681   34.   Lusvarghi, S., Durell, S. R. & Ambudkar, S. V. Does the ATP-bound EQ mutant
682   reflect the pre- or post-ATP hydrolysis state in the catalytic cycle of human P-
683   glycoprotein (ABCB1)? *FEBS Lett.* (2021). doi:10.1002/1873-3468.14054
684   35.   Hofmann, S. *et al.* Conformation space of a heterodimeric ABC exporter under
685   turnover conditions. *Nature* **571**, 580–583 (2019).
686   36.   Jin, M. S., Oldham, M. L., Zhang, Q. & Chen, J. Crystal structure of the multidrug

687 688		transporter P-glycoprotein from Caenorhabditis elegans. *Nature* **490**, 566–569 (2012).
689 690 691	37.	Dastvan, R., Mishra, S., Peskova, Y. B., Nakamoto, R. K. & Mchaourab, H. S. Mechanism of allosteric modulation of P-glycoprotein by transport substrates and inhibitors. *Science (80-.).* **364**, 689–692 (2019).
692 693 694	38.	Siarheyeva, A., Liu, R. & Sharom, F. J. Characterization of an asymmetric occluded state of P-glycoprotein with two bound nucleotides: Implications for catalysis. *J. Biol. Chem.* **285**, 7575–7586 (2010).
695 696	39.	Zivanov, J. *et al.* New tools for automated high-resolution cryo-EM structure determination in RELION-3. *Elife* **7**, (2018).
697 698 699	40.	Zivanov, J., Nakane, T. & Scheres, S. H. W. Estimation of high-order aberrations and anisotropic magnification from cryo-EM data sets in RELION-3.1. *IUCrJ* **7**, 253–267 (2020).
700 701	41.	Rohou, A. & Grigorieff, N. CTFFIND4: Fast and accurate defocus estimation from electron micrographs. *J. Struct. Biol.* **192**, 216–221 (2015).
702 703	42.	Pettersen, E. F. *et al.* UCSF Chimera - A visualization system for exploratory research and analysis. *J. Comput. Chem.* **25**, 1605–1612 (2004).
704 705	43.	Grant, T., Rohou, A. & Grigorieff, N. cisTEM, user-friendly software for single-particle image processing. *Elife* **7**, (2018).
706 707 708	44.	Ramlaul, K., Palmer, C. M., Nakane, T. & Aylett, C. H. S. Mitigating local over-fitting during single particle reconstruction with SIDESPLITTER. *J. Struct. Biol.* **211**, (2020).
709 710	45.	Wood, C. *et al.* Collaborative computational project for electron cryo-microscopy. *Acta Crystallogr. Sect. D Biol. Crystallogr.* **71**, 123–126 (2015).
711 712	46.	Emsley, P., Lohkamp, B., Scott, W. G. & Cowtan, K. Features and development of Coot. *Acta Crystallogr. Sect. D Biol. Crystallogr.* **66**, 486–501 (2010).
713 714 715	47.	Liebschner, D. *et al.* Macromolecular structure determination using X-rays, neutrons and electrons: Recent developments in Phenix. *Acta Crystallogr. Sect. D Struct. Biol.* **75**, 861–877 (2019).
716 717 718	48.	Croll, T. I. ISOLDE: A physically realistic environment for model building into low-resolution electron-density maps. *Acta Crystallogr. Sect. D Struct. Biol.* **74**, 519–530 (2018).
719 720	49.	Pettersen, E. F. *et al.* UCSF ChimeraX: Structure visualization for researchers, educators, and developers. *Protein Sci.* **30**, 70–82 (2021).
721	50.	The PyMOL Molecular Graphics System, Version 2.0 Schrödinger, LLC.
722 723 724	51.	Staritzbichler, R., Anselmi, C., Forrest, L. R. & Faraldo-Gómez, J. D. GRIFFIN: A versatile methodology for optimization of protein-lipid interfaces for membrane protein simulations. *J. Chem. Theory Comput.* **7**, 1167–1176 (2011).
725 726 727	52.	Best, R. B. *et al.* Optimization of the additive CHARMM all-atom protein force field targeting improved sampling of the backbone φ, ψ and side-chain χ1 and χ2 Dihedral Angles. *J. Chem. Theory Comput.* **8**, 3257–3273 (2012).
728 729	53.	Klauda, J. B. *et al.* Update of the CHARMM All-Atom Additive Force Field for Lipids: Validation on Six Lipid Types. *J. Phys. Chem. B* **114**, 7830–7843 (2010).
730 731	54.	Jeschke, G. DEER Distance Measurements on Proteins. *Annu. Rev. Phys. Chem.* **63**, 419–446 (2012).
732	55.	Jeschke, G. & Polyhach, Y. Distance measurements on spin-labelled

733   biomacromolecules by pulsed electron paramagnetic resonance. *Phys. Chem.*
734   *Chem. Phys.* **9**, 1895–1910 (2007).

735 56. Jo, S., Kim, T., Iyer, V. G. & Im, W. CHARMM-GUI: A web-based graphical user
736   interface for CHARMM. *J. Comput. Chem.* **29**, 1859–1865 (2008).

737 57. Qi, Y. *et al.* CHARMM-GUI DEER facilitator for spin-pair distance distribution
738   calculations and preparation of restrained-ensemble molecular dynamics
739   simulations. *J. Comput. Chem.* **41**, 415–420 (2020).

740

741   **TABLES**

742

743   **Table 1. Data collection and refinement statistics**

Refinement		
Lengths (Å)	101.66, 151.44, 97.43	
Atoms	19813 (Hydrogens: 9926)	
Residues	Protein: 1236	
Water	0	
Resolution (Å)	3.5	
Resolution Estimates (Å)	Masked	Unmasked
d FSC model (0/0.143/0.5) (Å)	2.8/3.1/6.1	3.0/3.1/6.4
B-factors (Å^2)		
Iso/Aniso (#)	9887/0	
Protein (min/max/mean)	12.04/113.39/61.00	
Bonds (RMSD)		
Length (Å) (# > 4σ)	0.007	
Angles (°) (# > 4σ)	1.199	
Validation		
MolProbity score	1.46	
Clash score	0.86	
Ramachandran plot (%)		
Outliers	0	
Allowed	9.0	
Favored	90.02	
Rotamer outliers (%)	1.54	
Model vs. Data		
CC (mask)	0.69	
CC (box)	0.61	
CC (peaks)	0.51	
CC (volume)	0.65	

744
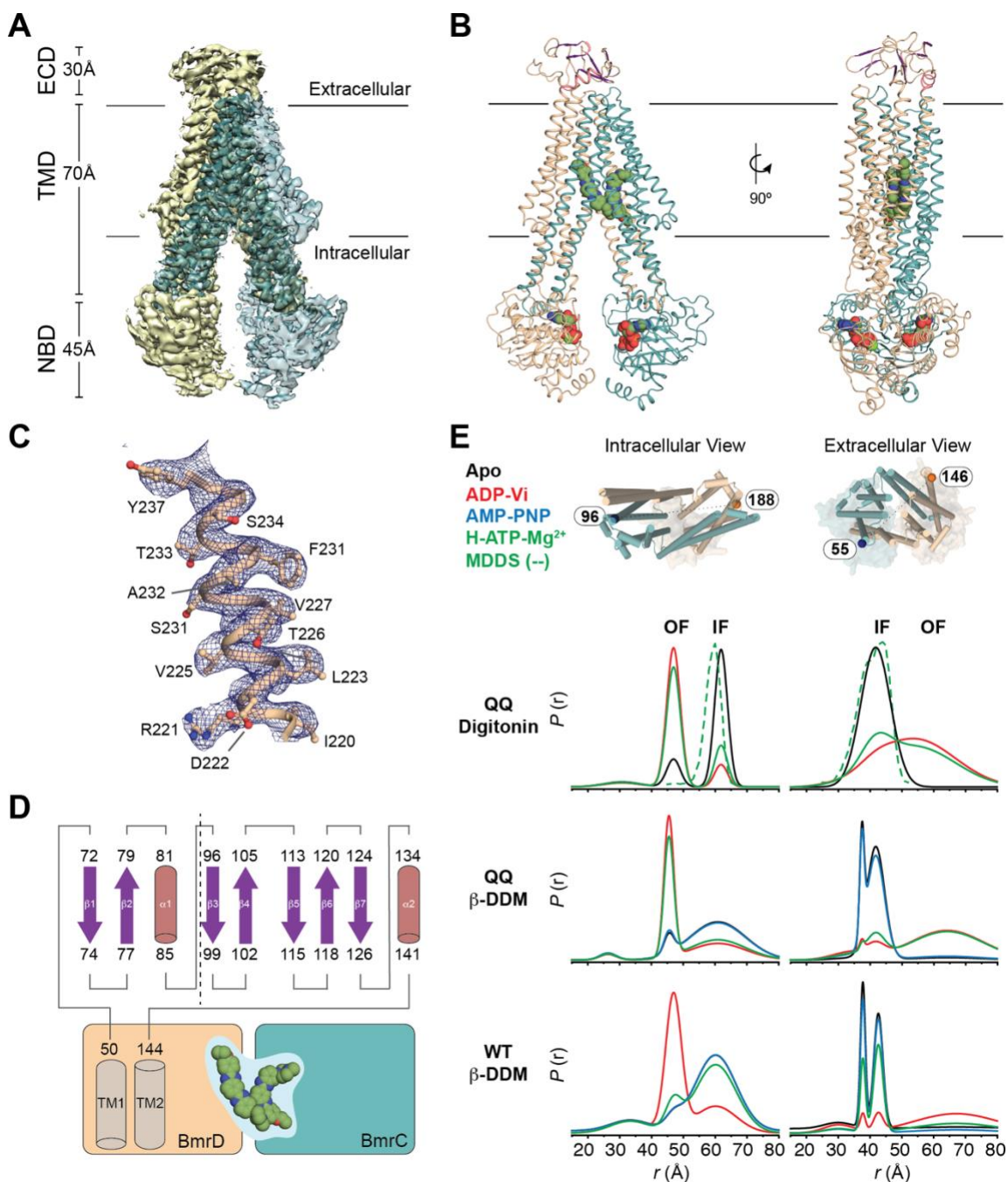
FIGURES

Figure 1

Figure 1. Structure of BmrCD[D500Q/E592Q] in complex Hoecsht-33342 and ATP. A) Cryo-EM map and **B)** model of BmrCD[D500Q/E592Q] (BmrCD-QQ) bound to ATP and Hoecsht-33342 (BmrCD-QQ[H/ATP]) highlighting the geometry and arrangement of the transmembrane domains (TMDs) and nucleotide binding domains (NBDs) relative to the extracellular domain insertion (ECD) and the membrane. **C)** Representative density of the

755   3.5Å resolution structure show in (**A**) and model corresponding to transmembrane helix
756   3 from BmrD (TM3^D). **D)** Topology of the ECD observed in BmrCD-QQ$^{H/ATP}$ relative to the
757   TMD. **E)** DEER distance measurements for spin label pairs on the intracellular and
758   extracellular regions of the TMD in the Cysteine-free background (WT*) or the QQ mutant
759   of BmrCD and in the presence of different substrates. The MDDS-derived distance
760   distributions calculated for the cryo-EM model in (**B**) is overlaid with the DEER derived
761   distance distributions.
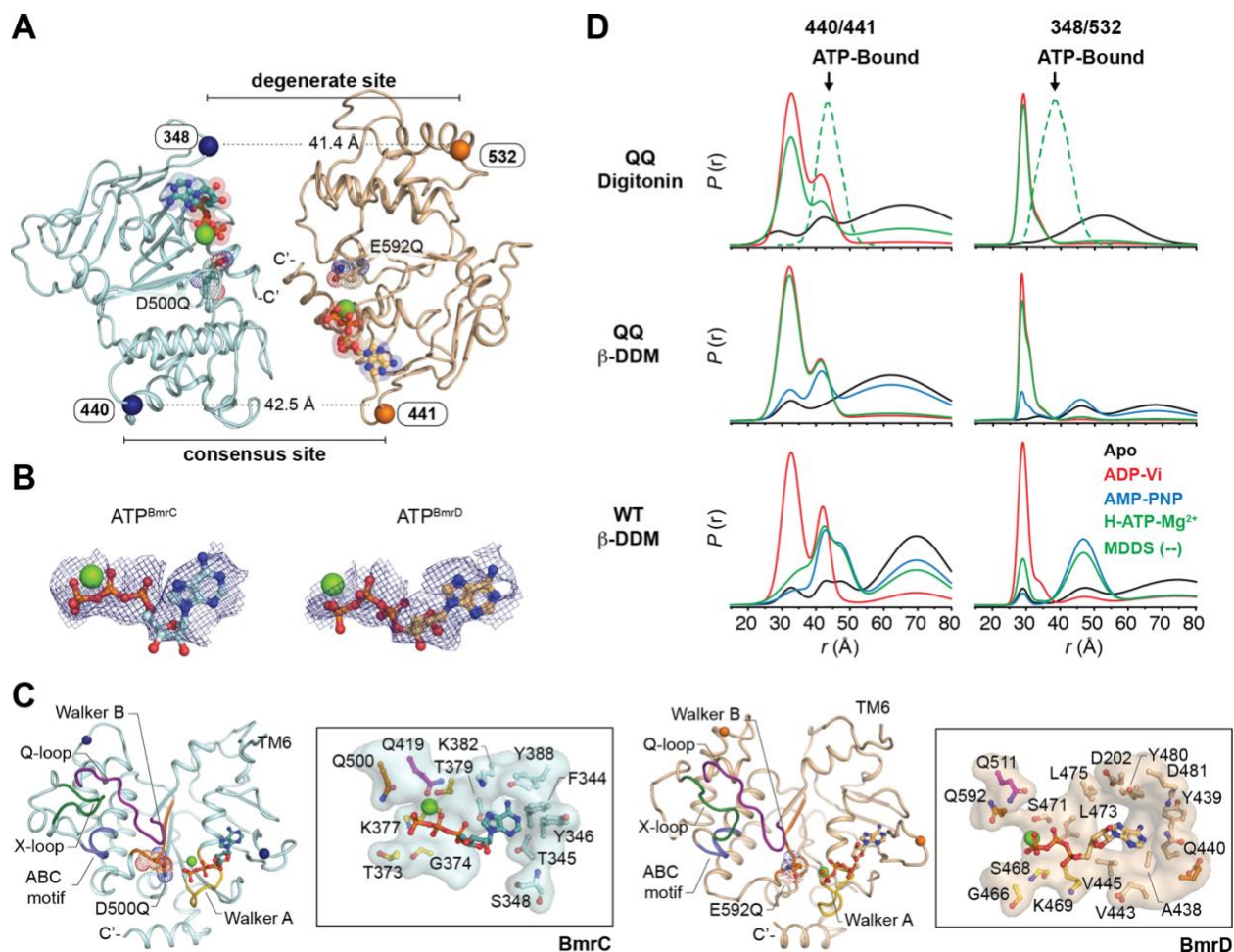
Figure 2

Figure 2. Symmetric geometry of ATP-bound NBSs in BmrCD-QQ$^{H/ATP}$. A) Overview of the nucleotide binding domains in the cryo-EM structure of BmrCD-QQ$^{H/ATP}$. **B)** Electron Potential Density corresponding to ATP bound in the BmrC (left) and BmrD (right) chains with symmetric geometries. **C)** Comparison of NBD secondary structure in BmrC (left) and BmrD (right) highlighting the architecture of conserved motifs and the orientations of ATP molecules relative to the position of the catalytic base (D500Q in BmrC; E592Q in BmrD). In the inset, an overview of the atomic features of the ATP binding pockets of each are shown with residues from conserved motifs colored the same. The orientations shown are of the same view in which BmrD was superimposed onto BmrC to highlight the symmetry of the ATP conformation in each. **D)** DEER distance distributions for spin labeled pairs in C-less wild-type and QQ-mutant of BmrCD consensus (440/441) and degenerate (348/532) nucleotide binding sites under varying conditions. Superimposed in dashed green lines (MDDS) are the distance distributions predicted by the structure.

779   **Figure 3**
780
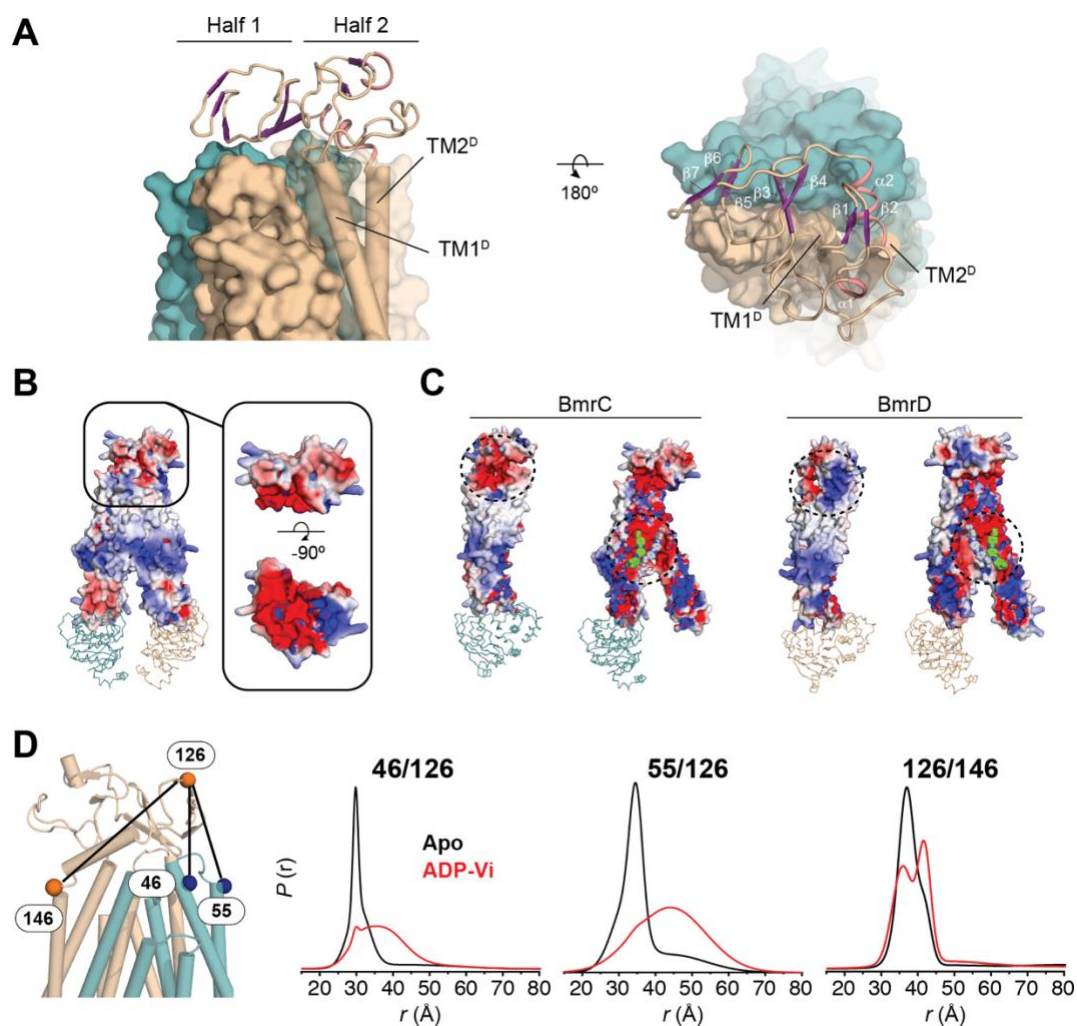
781

782   **Figure 3. A dynamic role of the ECD in BmrCD-QQ$^{H/ATP}$ catalysis. A)** Orientation of
783   the ECD in BmrCD-QQ$^{H/ATP}$ relative to its TMD. **B)** Electrostatic distribution over the
784   surface of the BmrCD-QQ$^{H/ATP}$ ECD and its interactions with **C)** BmrC (left) and BmrD
785   (right). **D)** ECD/TMD spin labeled pairs generated in C-less BmrCD to monitor the ATP-
786   dependent dynamics of the ECD.
787
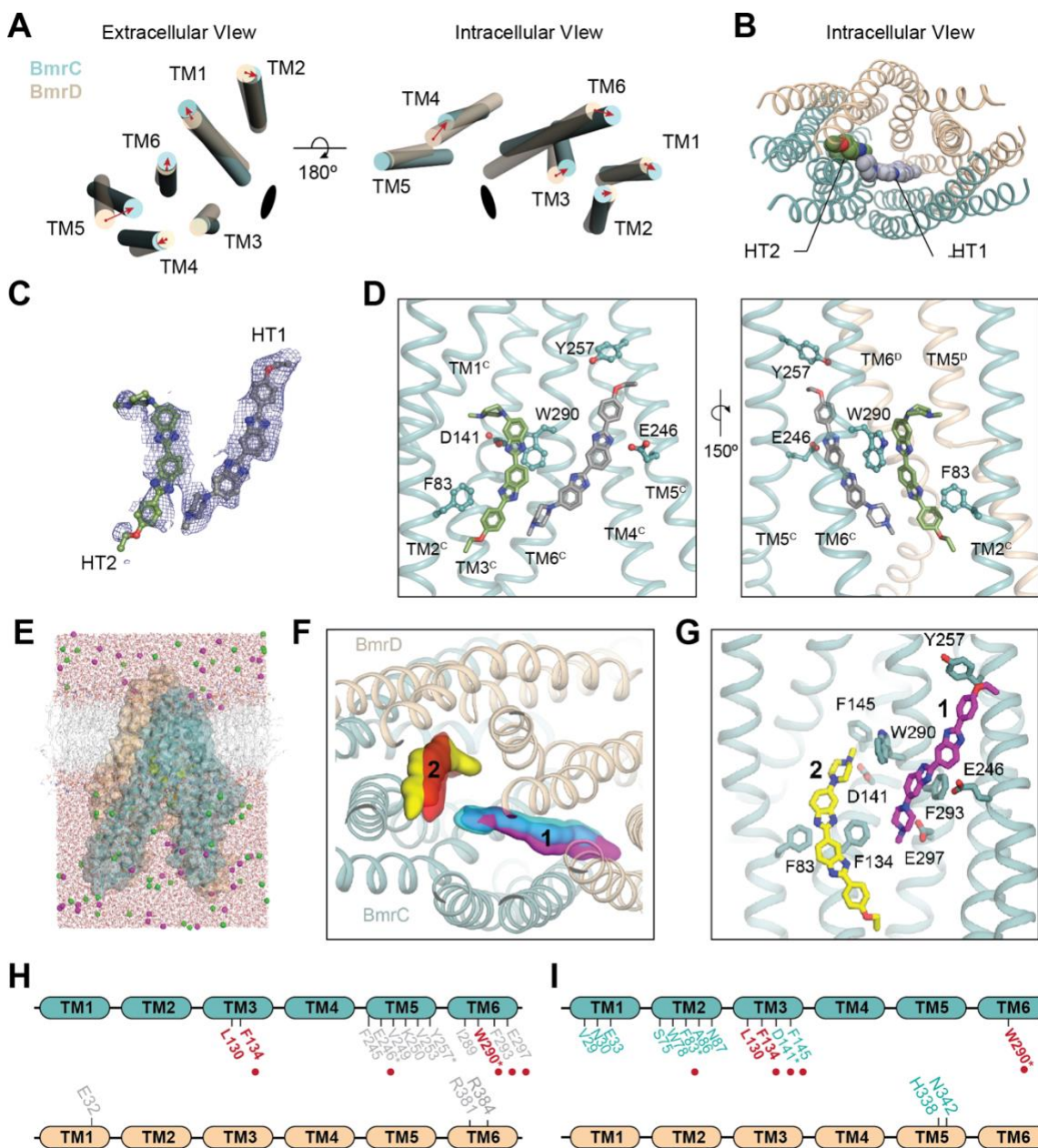
Figure 4

Figure 4. Asymmetric binding of Hoecsht-33342 in BmrCD-QQ[H/ATP]. A) Superposition of BmrD transmembrane helices (TM1-6) onto BmrC shown from the extracellular (left) and intracellular (right) gates to highlight asymmetry in the TM arrangement observed in the structure of BmrCD. Red arrows correspond to the movement of each TM in BmrC relative to its position in BmrD. Black ellipse corresponds to the symmetry axis around which BmrD was rotated during superposition. **B)** Intracellular view of the arrangement of two molecules of Hoecsht-33342 (HT1 and HT2) modelled in the TMD of BmrCD. **C)** Electron Potential Density observed corresponding to HT1 and HT2 and **D)** their positioning inside of the binding pocket. **E)** All-atom simulation system, comprising the transmembrane domain of BmrCD with two Hoechst molecules placed into the proposed

binding site, in a POPC lipid bilayer and 100 mM NaCl (BmrC, blue surface/cartoons; BrmD, orange surface/cartoons; Hoechst, yellow spheres; lipid, gray lines; water, red lines; sodium, magenta spheres; chloride, green spheres). **F)** Density maps calculated from the MD trajectories for each Hoechst molecule are overlaid onto the starting cryo-EM structure (magenta/red surfaces derive from one trajectory and cyan/yellow from the other). **G)** Snapshot representative of the calculated density maps, highlighting the configuration of the two Hoechst molecules and their seemingly most significant sidechain contacts with BmrC. Hydrogen atoms are omitted for clarity. Probability distributions for each of these interaction distances are shown in Supp. Fig. 6. The HT1 and HT2 specific interactions are summarized in **H)** and **I)**, respectively and mapped onto the respective chains colored the same as in (**A**) and (**B**). Residues colored in red are observed interacting with both molecules in the cryo-EM structure. Residues with an asterisk were mutated in the study here and are shown as sticks in (**D**). Red spheres correspond to residues identified as interacting with HT1 or HT2 in both the cryo-EM structure and all-atom simulation.
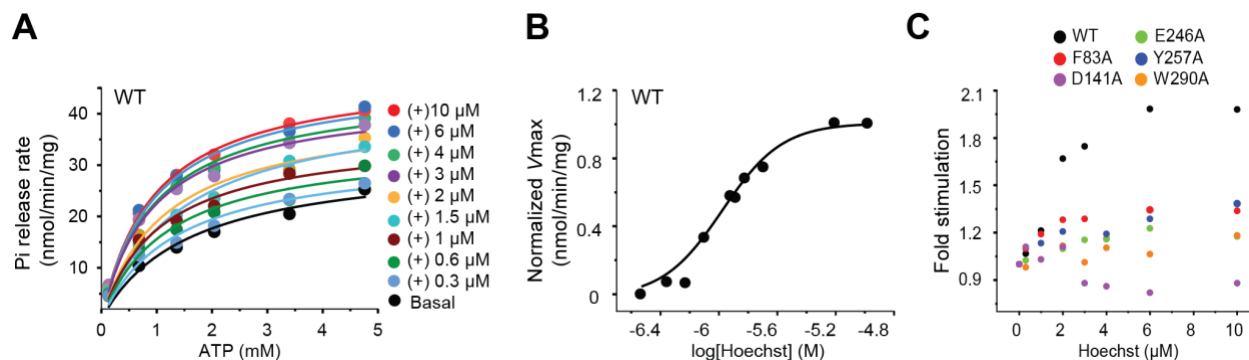
Figure 5

Figure 5. Cooperative stimulation of ATP turnover by Hoechst-33342. A) Hoechst-33342 concentration dependent stimulation of ATPase activity in wild-type C-less BmrCD (WT). **B)** Dose-response curve for Hoechst-mediated stimulation of ATpase activity highlighting cooperativity in wild-type C-less BmrCD (WT). The data is the average of two biological repeats and six technical repeats. **C)** Comparison of Hoechst-stimulated ATPase activity relative to basal activity (fold stimulation) in WT* and alanine mutants of BmrCD. Mutants selected are of a subset of residues observed interacting with Hoechst-33342 in the BmrCD-QQ$^{H/ATP}$ cryo-EM structure (see Figure 4).

Supplementary Materials

Supplemental Tables

Supplemental Table 1. RMSD analysis of domain architecture in BmrCD

	RMSD (Å)
TMD	3.07
TM1	2.2
TM2	1.41
TM3	8.58
TM4	4.99
TM5	2.07
TM6	1.86
ICLs	2.36
ICL1	1.32
ICL2	1.19
NBD	2.85

TMD: transmembrane domain; ICLs: intracellular loops; NBD: nucleotide-binding domain

Supplemental Table 2. BmrCD vs. TmrAB RMSD Analysis

			TMD RMSD (Å)				NBD RMSD (Å)	
		overall	A vs. D	B vs. D	A vs. C	B vs. C	A vs. D	B vs. C
IO	*5mkk*	5.025	2.639	3.513	3.776	2.775	2.099	1.232
	6raf	5.424	2.285	3.612	4.247	3.813	2.232	1.394
	6rag	3.624	2.253	2.442	3.133	2.002	1.851	1.55
	6ran	3.404	2.159	2.293	2.927	1.882	2.316	1.467
OO	*6rah*	7.589	5.976	6.563	6.948	6.268	2.765	1.434
	6rai	6.731	4.731	5.297	5.557	3.097	2.683	1.592
	6raj	7.607	5.937	6.499	6.943	6.407	2.773	1.648
	6rak	6.757	4.799	5.371	5.696	3.291	2.687	1.627
	6ral	6.399	4.381	4.899	5.225	3.011	2.824	1.593
	6ram	6.059	4.029	4.271	4.822	2.887	2.712	1.373

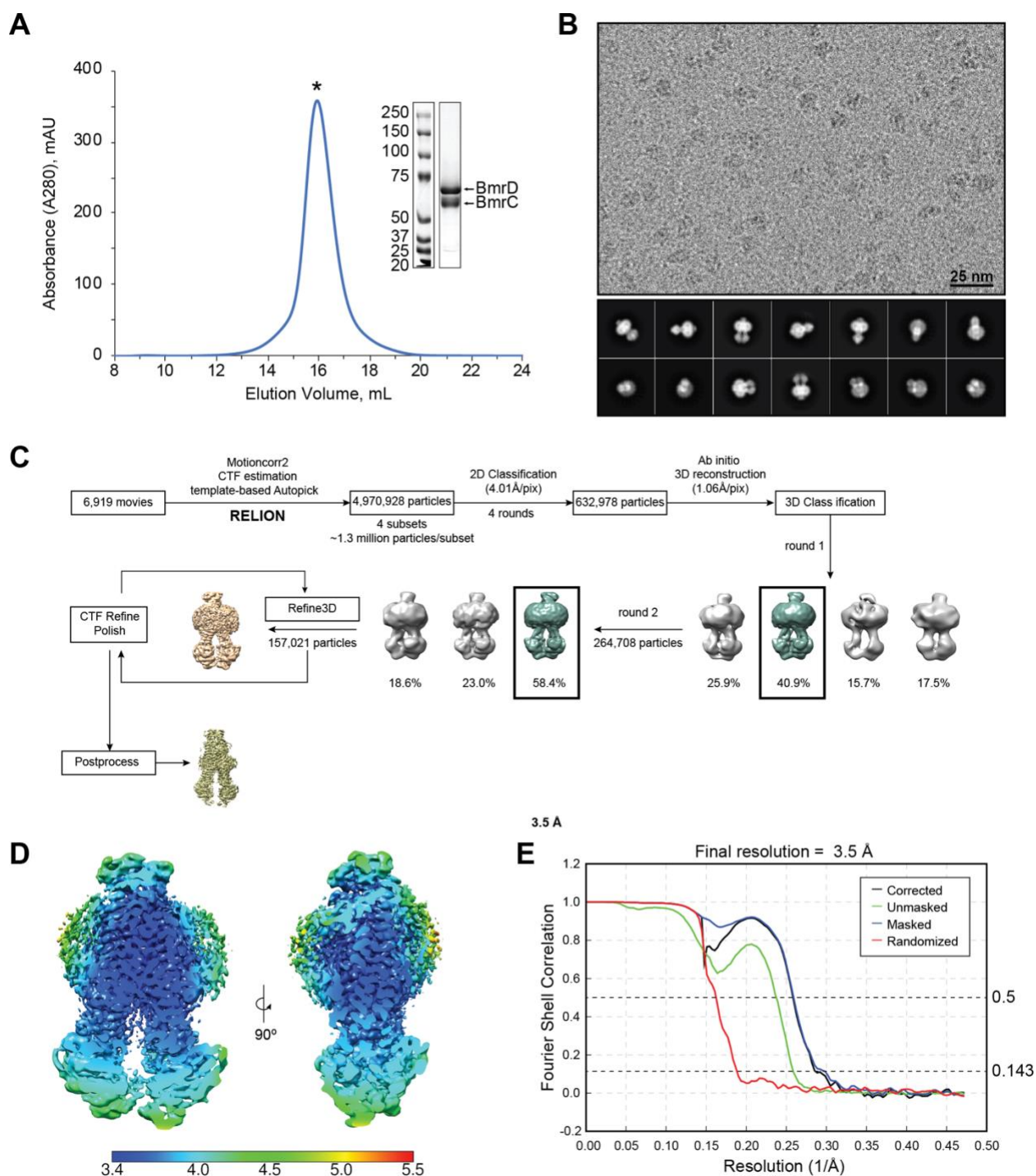IO: inward-facing open; OO: outward-facing open or occluded

27

838 **Supplemental Figures**
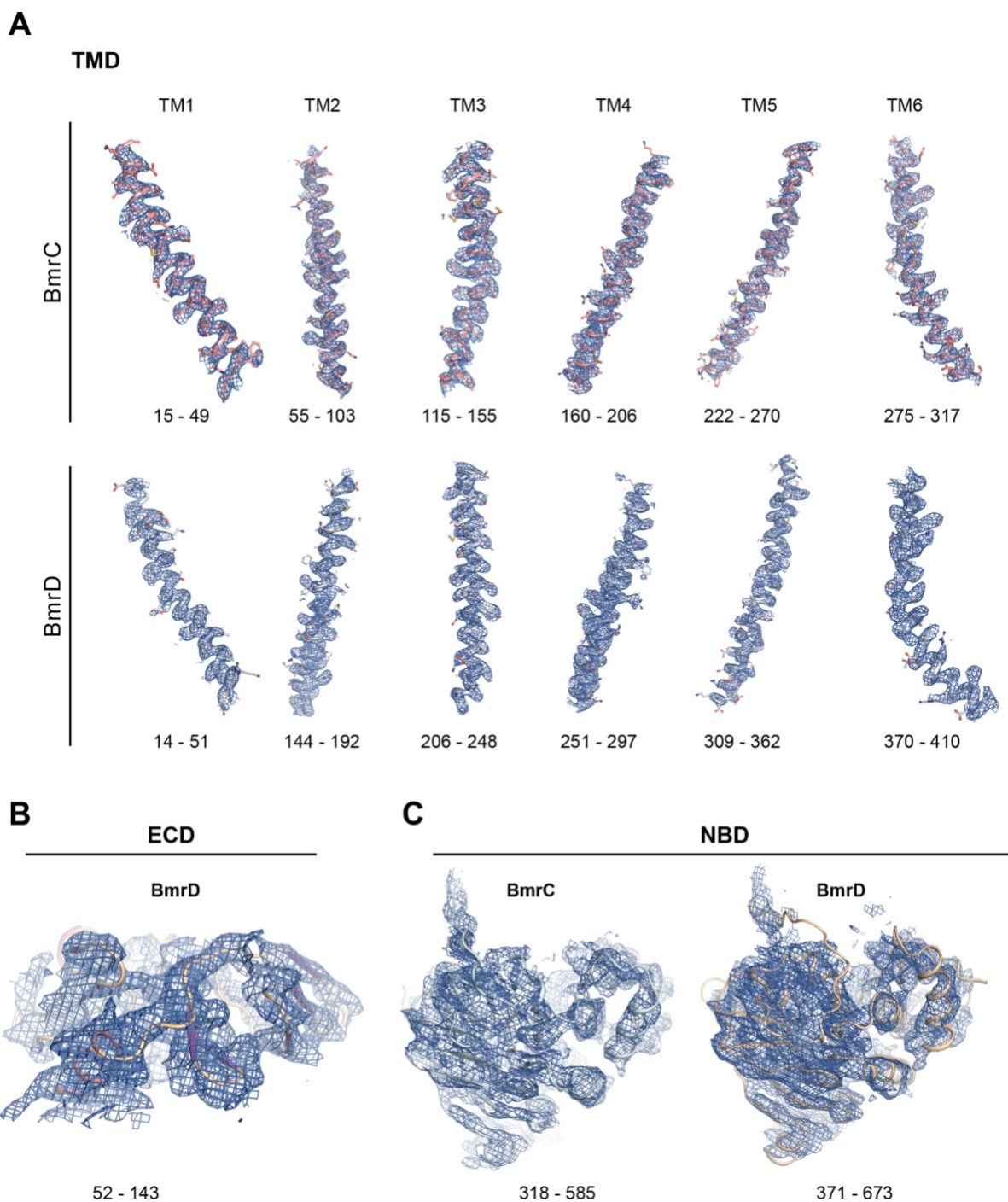
839 **Supplementary Figure 1**

840

841 **Supplementary Figure 1. Cryo-EM data processing of BmrCD-QQ in the Hoechst-**
842 **33342 and ATP/Mg bound state. A)** Chromatogram and SDS-PAGE analysis of the
843 peak composition for BmrCD-QQ purified by size exclusion chromatography over a

28

844   Superose 6 column equilibrated in 0.02% digitonin containing buffer prior to sample
845   preparation for cryo-EM data collection. **B)** Representative micrograph and 2D
846   classification results from cryo-EM data collected for BmrCD-QQ in the presence of
847   equimolar ATP/MgCl$_2$ and excess Hoechst-33342. **C)** Flowchart of data processing in
848   RELION 3.1[40]. **D)** A slice through the EM volume colored according to local resolution. **E)**
849   FSC curves calculated in RELION 3.1.
850

851   **Supplementary Figure 2**

852

853   **Supplementary Figure 2. Cryo-EM map data quality.** Model and corresponding density
854   of BmrCD-QQ **A)** transmembrane helices (TM1-6), **B)** extracellular domain (ECD), and
855   **C)** nucleotide binding domains (NBD).
856

857 **Supplementary Figure 3**

858
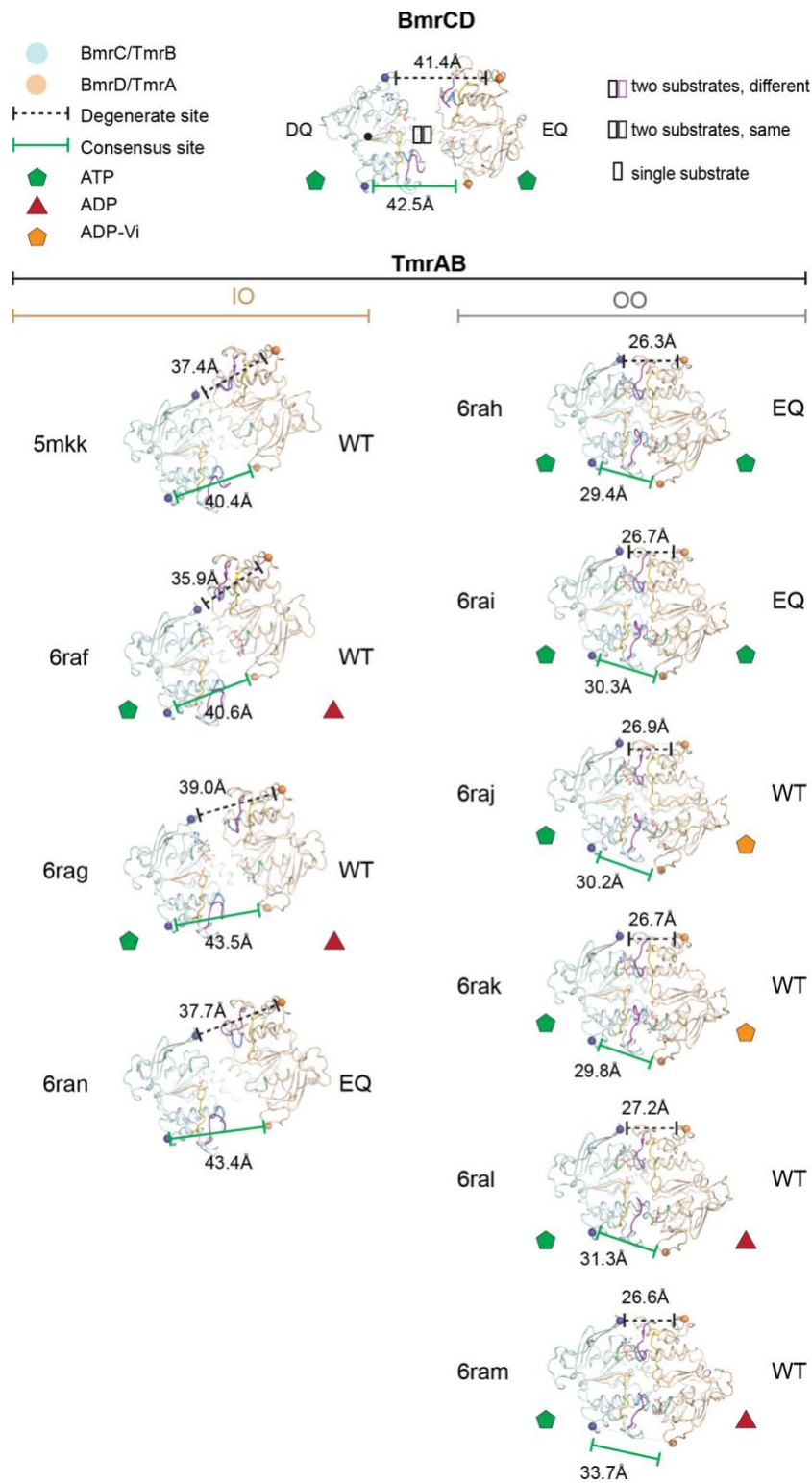
Supplementary Figure 3. Analysis of NBD symmetry in BmrCD compared to TmrAB. Comparison of NBD geometry between BmrCD and different states of TmrAB

861   determined by x-ray crystallography (PDB ID: 5mkk[18]) and cryo-EM[2]. The noncanonical
862   NBD in BmrC and TmrB are colored *cyan*, whereas the consensus NBDs of BmrD and
863   TmrA are colored *orange*. The orientations shown are relative to BmrCD and in which
864   TmrB was aligned to BmrC (marked with a black dot in the center to denote the reference
865   orientation). Structures of TmrAB are shown grouped by architectures adopting inward-
866   facing open states (IO) or outward-facing states (OO).

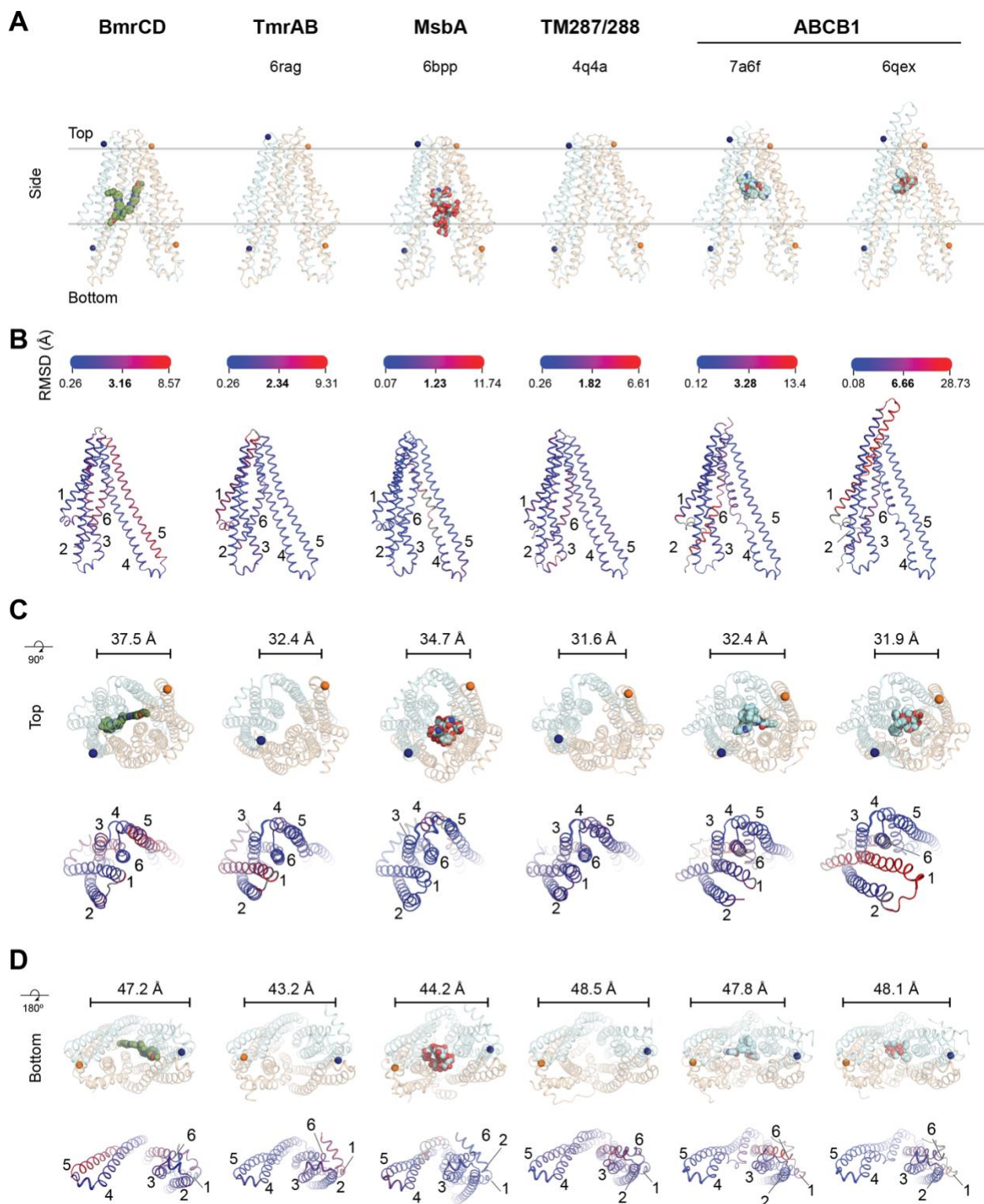867 **Supplementary Figure 4**

868
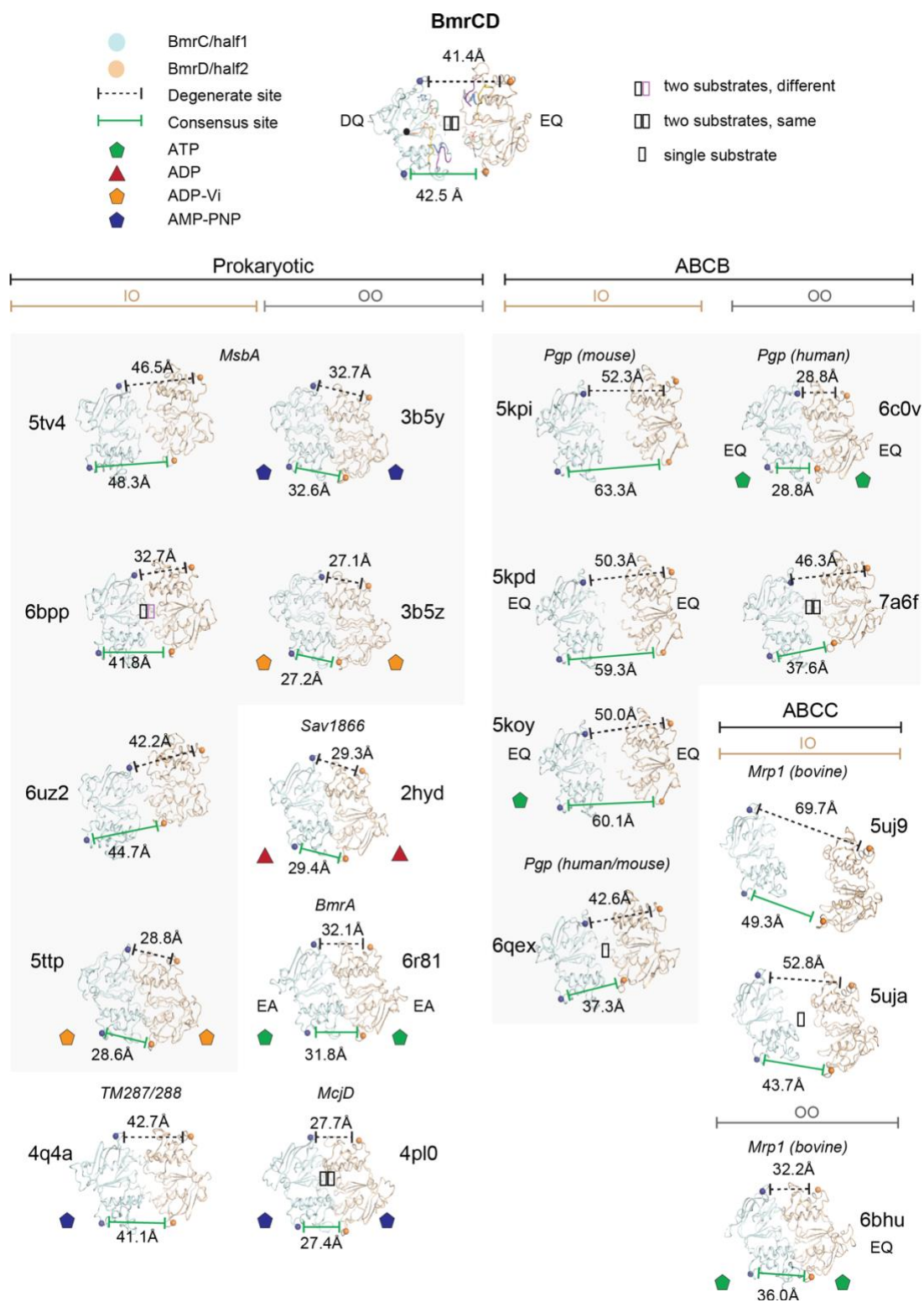
869 **Supplementary Figure 4. Analysis of NBD symmetry between BmrCD and other**
870 **representative ABC transporters.** Comparison of NBD geometry between BmrCD and

871   structures of related ABC transporters from bacteria (MsbA PDB IDs: 5tv4[19], 6bpp[20],
872   6uz2[21], 3b5y[23], and 3b5z[23], TM2987/288 PDB ID: 2hyd[24], BmrA PDB ID: 6r81
873   (unpublished); McjD PDB ID: 4pl0[6]) as well as from the ABCB (or Pgp) and ABCC families
874   . The noncanonical NBDs, or the first NBD (half 1) in homomeric or single polypeptide
875   transporters, are colored *cyan*, whereas the consensus NBDs, or the second NBD in
876   homomeric or single polypeptide transporter, are colored *orange*. The orientations shown
877   are relative to BmrCD in which half 1 was aligned to BmrC (marked with a black dot in the
878   center to denote the reference orientation). Structures are shown grouped by
879   architectures adopting inward-facing open states (IO) or outward-facing states (OO).
880

Supplementary Figure 5

Supplementary Figure 5. Analysis of BmrCD TMD in comparison to closely related ABC exporters. A) Overview of the transmembrane domain (TMD) geometry in BmrCD

885   and related inward-facing states of related prokaryotic (PDB IDs: 6rag[2], 6bpp[20], and
886   4q4a[22]) and occluded human ABC transporters bound with inhibitor (PDB ID: 7a6f[13]) or
887   substrate (PDB ID: 6qex[12]). The extracellular domain of BmrD and both nucleotide binding
888   domains have been omitted for clarity. Sites on the extracellular and intracellular gates
889   labeled for DEER experiments in BmrCD and the homologous residues in the related
890   exporters are shown as spheres and colored the same as Figures 1 of the main text,
891   where the non-canonical nucleotide-binding site containing half are colored *cyan* (BmrC
892   in BmrCD), and the canonical NBS containing half are colored *orange* (BmrD in BmrCD).
893   **B)** The Cα RMSD resulting from superposition of each TMD half within each structure is
894   mapped onto the structure of the non-canonical half. The scale bar above represents the
895   minimum, median, and maximum RMSD calculated for each superposition. The geometry
896   and RMSD distribution in each are shown for the **C)** outside-facing (top) and **D)** inside-
897   facing (bottom) regions of the TMDs to highlight the variation in asymmetry in each
898   structure. Numbers in the RMSD representation correspond to the transmembrane helix
899   number.
900
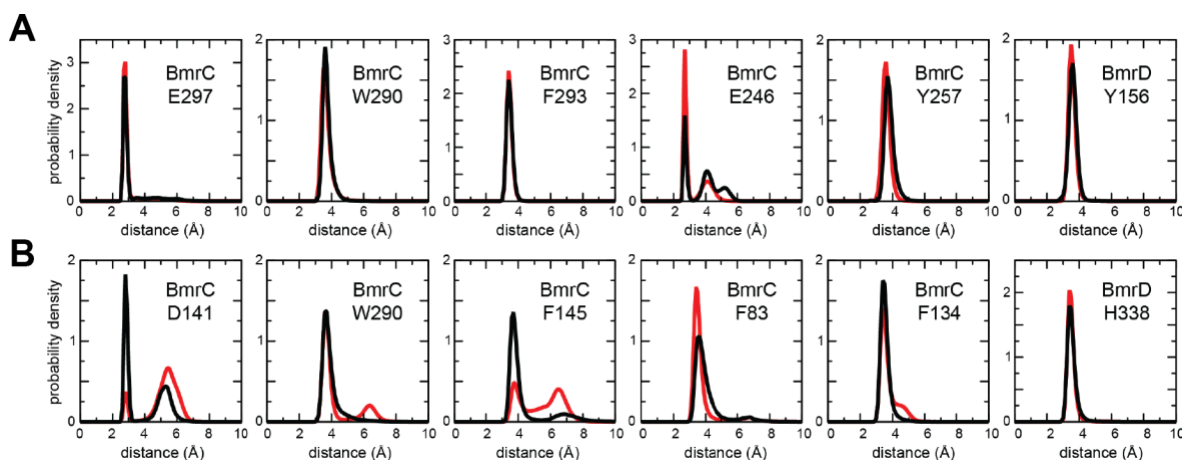
Supplementary Figure 6

Supplementary Figure 6. Examination of the Hoechst-33342 binding pose with MD simulations. Data is shown for two independent MD trajectories (*black*, *red*) of the BmrCD construct shown in Fig. 4E, with two Hoechst molecules bound. **A)** Quantification of ionic and aromatic interactions between Hoechst molecule '1' and residues in BrmC, in terms of probability distributions of the minimum distance between the ligand and each sidechain (excluding hydrogens). The only significant contact of Hoechst molecule '1' with BrmD is also indicated. **B)** Same as **A)**, for molecule '2'.
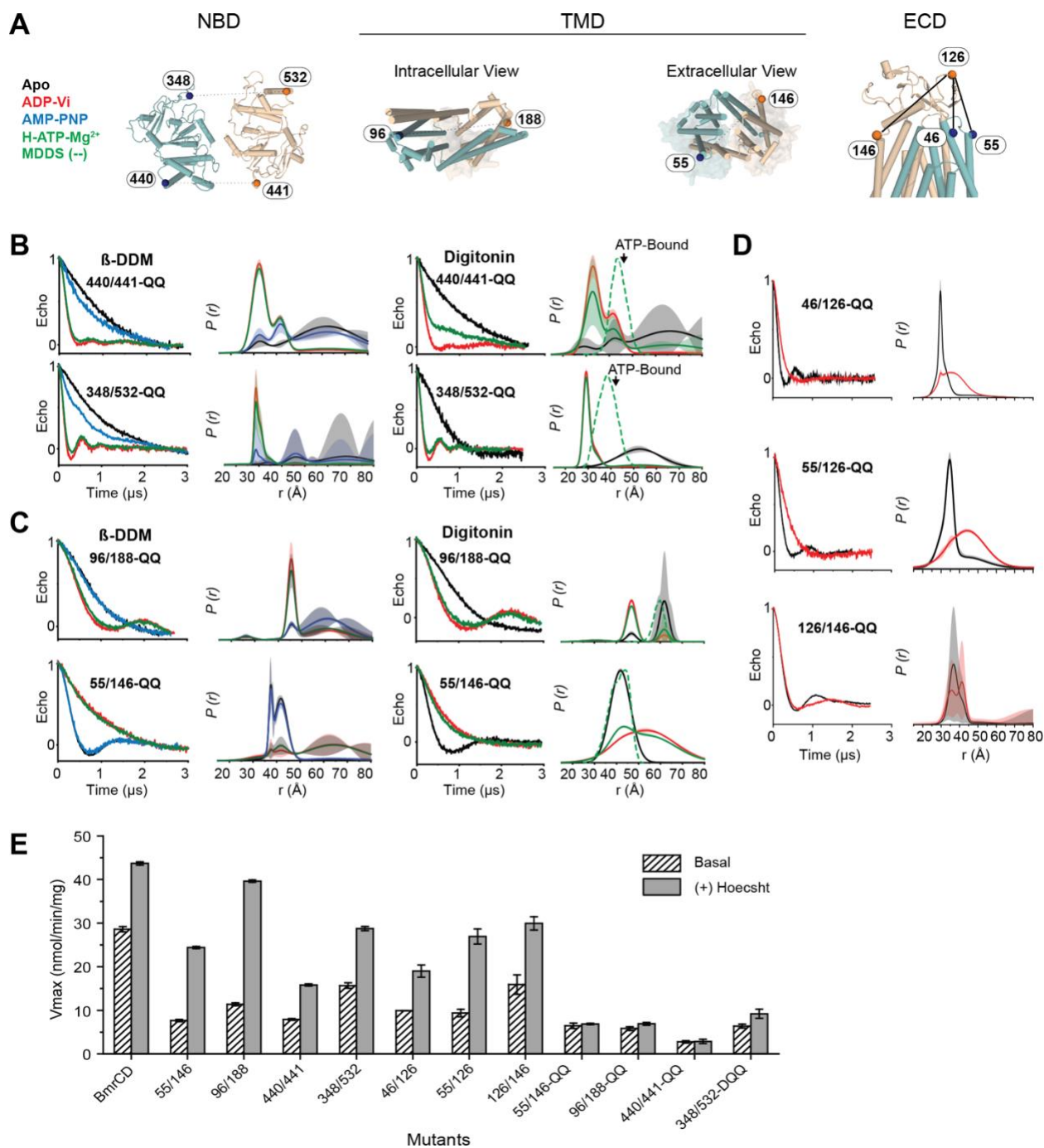
Supplementary Figure 7

Supplementary Figure 7. A) Cartoon representations of BmrCD subdomains highlighting the position of spin-labeled cysteine pairs generated in the nucleotide binding domain (NBD), transmembrane domain (TMD), and the extracellular domain (ECD). DEER decay signals and distance distributions for spin-labeled Cysteine pairs generated in the **B)** NBD, **C)** TMD, and **D)** ECD for wild-type and mutant (QQ) C-less BmrCD. The shaded regions represent confidence bands. **E)** Quantification of maximal ATPase rates (*V*max) in wild-type and C-less spin-label mutants of BmrCD.